JM PAPERS

Self-similarity in over-tripped turbulent boundary-layer flows

Zhanqi Tang[1,2,†] **and Nan Jiang**[1,2]

[1]Department of Mechanics, Tianjin University, Tianjin 300350, China

[2]Tianjin Key Laboratory of Modern Engineering Mechanics, Tianjin 300350, China

The scaling universality of structure functions is studied for artificially thickened turbulent boundary-layer flows in over-tripped impacts by using hot-wire measurement datasets. The self-similarity behaviours in the inner and outer regions are examined from the viewpoint of different flow mechanisms. In the inner region, the relative ratios between structure functions for the energy-containing range of scales exhibit universality behaviour, in accordance with Townsend's attached eddy hypothesis. This universality of the energy-containing range of scales extends further away from the wall by increasing the tripping intensity. On the other hand, the impact of the external intermittency on the self-similarity of small-scale turbulence is examined through the intermittent zone in over-tripped conditions. Towards the boundary-layer edge, the structure functions exhibit a growing departure from self-similarity and analytical prediction, and it is demonstrated that the departure is primarily due to external intermittency. Moreover, based on the conditional statistics concentrated in the turbulent regimes, it is revealed that the small scales in the turbulence regime are homogenized in a self-similar behaviour, which is independent of the current tripping conditions.

Key words: turbulent boundary layers

1. Introduction

1.1. *Extended self-similarity*

Turbulent flows are characterized by non-Gaussian, intermittent fluctuations over a wide range of different scales (Frisch 1995; Pope 2000). Based on the assumption that the statistical property of the velocity fields is locally isotropic, Kolmogorov's similarity theory predicts that, at sufficiently large Reynolds numbers, the small-scale motions decouple from the large scales and are independent of the boundary or initial conditions,

† Email address for correspondence: zhanqitang@tju.edu.cn

which can be expressed as structure functions

$$\langle (\Delta_r u)^n \rangle \propto r^{\xi_n}, \tag{1.1}$$

where $\Delta_r u = u(x + r) - u(x)$ is the velocity increment, $u(x + r)$ and $u(x)$ are velocities along the streamwise direction at two points separated by a spatial distance r, $\langle \ \rangle$ represents averaged quantities and ξ_n is the scaling exponent. This universality hypothesis indicates that the statistical properties of the velocity fields are self-similar within the inertial range, $\eta \ll r \ll L$, where η is the dissipation scale and L is the integral scale of turbulent motions. While the possible existence of universal scaling exponents ξ_n is one of the most significant headways of turbulence, a scaling exponent deviation from the Kolmogorov prediction $\xi_n = n/3$ has been widely reported, specifically for the higher-order statistics (Anselmet *et al.* 1984; Frisch 1995; Sreenivasan & Antonia 1997). The 'anomalous' deviation behaviour from the Kolmogorov scaling has been attributed to the non-Gaussian, strong intermittent fluctuations, which are often known as internal intermittency (Landau & Lifshitz 1963).

Otherwise, extensive investigations have been devoted to the existence of universal scaling laws of $\langle (\Delta_r u)^n \rangle$ for various kinds of turbulent flows by employing the so-called extended self-similarity (ESS) hypothesis (Benzi *et al.* 1993*a,b*). Rather than pursuing the universal scaling exponents ξ_n of the *n*th-order structure function for the inertial subrange (ISR) scales, ESS describes the relative scaling exponent of one given structure function against another as

$$\langle (\Delta_r u)^n \rangle \propto \langle |\Delta_r u|^3 \rangle^{\xi_n}, \tag{1.2}$$

where the scaling ξ_n is computed relative to the third-order structure function of the modulus of the velocity increments. The self-similarity form of the ISR scaling properties in ESS form following (1.2) has been consolidated to hold for various turbulent flows and at high as well as low Reynolds numbers (Grossmann, Lohse & Reeh 1997; Yang *et al.* 2016*b*).

In wall turbulence, the dominance of energy-containing range (ECR) scales in the logarithmic region is argued to challenge the scaling universality due to the wall boundedness conditions (Pope 2000). The popularity of the ECR scales, $y < r \ll \delta$ (where y and δ represent the wall-normal distance and boundary-layer thickness) has been reported in wall-bounded turbulence. Following Townsend's attached eddy hypothesis (Townsend 1976; Meneveau & Marusic 2013; Hu, Yang & Zheng 2019; Marusic & Monty 2019; Wang *et al.* 2021, 2022), the ECR scales of the normalized even-ordered longitudinal structure functions can be expressed as (Davidson, Nickels & Krogstad 2006; de Silva *et al.* 2015, 2017)

$$\langle (\Delta_r u_+)^{2p} \rangle^{1/p} = D_p \ln \left(\frac{r}{y} \right) + E_p, \tag{1.3}$$

where D_p and E_p are constants. The velocity is given in wall units by the subscript $+$ ($u_+ = u/u_\tau$, where u_τ is the friction velocity). The scaling behaviour by (1.3) in the ECR scales ($y < r \ll \delta$) was confirmed in the logarithmic region from high-Reynolds-number databases, and the scale extent was limited to the given wall-normal distance (Davidson *et al.* 2006; de Silva *et al.* 2015). The work of de Silva *et al.* (2017) further discerned the universality of the scaling for the ECR scales in the ESS framework. They examined the scaling behaviour of the even-order velocity structure functions $\langle (\Delta_r u_+)^{2p} \rangle^{1/p}$ for

wall-bounded turbulent flows as the expression

$$\langle (\Delta_r u_+)^{2p} \rangle^{1/p} = \frac{D_p}{D_m} \langle (\Delta_r u_+)^{2m} \rangle^{1/m} + E_p - \frac{D_p}{D_m} E_m. \tag{1.4}$$

By means of the ratio of D_p/D_m as extracted in (1.4), the further reaching universality of the ECR of scales was demonstrated in wall-bounded flows which span a wide range of Reynolds numbers and flow geometries (de Silva *et al.* 2017; Xia, Brethouwer & Chen 2018; Hu *et al.* 2019). Specifically, the universality was also observed at $Re_\tau \sim O(10^3)$ ($Re_\tau = u_\tau \delta/\nu$, ν is kinematic viscosity), which supports that the scaling for the ECR scales in (1.4) provides more precise measures to examine the structure functions at relatively lower Reynolds numbers.

1.2. *Over-tripped turbulent boundary layer*

In practical industrial applications, turbulent flows in wind turbines, pipelines, ships and aviation, are in the range of high Reynolds numbers. From the academic aspect, the characteristics of the turbulent boundary-layer (TBL) flows at high Reynolds numbers (Re_τ) have always been the focus for researchers (Marusic *et al.* 2010; Smits, McKeon & Marusic 2011; Marusic *et al.* 2013; Smits & Marusic 2013; Smits 2020). Admittedly, achieving high-Re_τ TBLs in a canonical form is an infrastructural and economic challenge. Instead, the artificially thickened TBL generated in a given wind tunnel is assumed as one of the cheaper/feasible approaches to mimic the high-Re_τ TBLs.

Since the pioneering work by Klebanoff & Diehl (1951) to artificially generate the TBL flows, numerous studies have been executed in this area by considering the impact of the inflow Reynolds number, tripping device, adaptation length and so on (Erm & Joubert 1991; Fernholz & Finleyt 1996; Castillo & Johansson 2002; Jiménez *et al.* 2008; Chauhan, Monkewitz & Nagib 2009; Schlatter & Örlü 2010*a*,*b*, 2012). For a certain inflow Reynolds number, incorporating some perturbation by the tripping devices at the leading edge of the flat plate is a generally accepted approach to promoting an earlier transition for the development of TBL flows (Erm & Joubert 1991; Fernholz & Finleyt 1996; Jiménez *et al.* 2008; Chauhan *et al.* 2009). A small perturbation by the tripping device results in an underdeveloped boundary layer. It is necessary to have a long enough adaptation region for the formation of a fully developed TBL with a high boundary-layer thickness. However, the requirement of a sufficiently long development length is not feasible in a common laboratory environment. On the other hand, for a test section of finite length, a strong perturbation at the leading edge will lead to an over-tripped boundary layer up to surprisingly high Reynolds numbers, by presenting a remarkably increased boundary-layer thickness in the adaptation region (Castillo & Johansson 2002; Schlatter & Örlü 2012; Marusic *et al.* 2015). Thus, it is more desirable to obtain an artificially thickened higher-Re_τ TBL by an elaborately appropriate trip design (Schlatter & Örlü 2010*a*, 2012).

A considerable effort has been dedicated to understanding the effects of an exact tripping device with different sizes and shapes on the boundary layer in the adaptation region (Hunt & Fernholz 1975). Rodríguez-López, Bruce & Buxton (2016*b*) proposed that the adaptive boundary layer could be generated through two mechanisms: wall driven and wake driven, by employing two families of tripping devices which are high aspect ratio uniformly distributed cylinders and low aspect ratio sawtooth fences. For the wall-driven mechanism, the inner structures drive the mixing of the obstacle's wake. On the other hand, the wake-driven mechanism is related to a long adaptation region where the inner

structures are reorganized under the influence of highly energetic wake motions. These proposed driven mechanisms have been further confirmed by assessing the geometry parameters of tripping devices, such as aspect ratio, blockage ratio and blockage at the wall (Rodríguez-López, Bruce & Buxton 2017*a*,*b*; Buxton, Ewenz Rocher & Rodríguez-López 2018).

Furthermore, to characterize the scaling in the adaptation region, Marusic *et al.* (2015) measured the spatial development of high-Re_τ TBL flows from the tripping threaded rods of different diameters. A significant difference was noted in the outer region under the tripping effects, and the influence on the outer region persists for more than 10 m along the streamwise direction. Tang *et al.* (2024) observed the deviation of the boundary layer from the canonical state, which is tripped by a set of transverse cylindrical rods with incremental diameters at the given inflow Reynolds number. They confirmed that the tripping effects are significant in the outer region by introducing large-scale energetic structures. These observations are consistent with the previous results that the threaded/cylindrical rods featured by the high wall blockage can trigger a long adaptation region by generating a prominent wake in the outer layer (Klebanoff & Diehl 1951; Chauhan *et al.* 2009; Sanmiguel Vila *et al.* 2017). These generated energetic wake motions dominate the outer region, which exerts a prominent modification on the external intermittency (Tang *et al.* 2024). Furthermore, these wake motions transport fluid across the entire wall-normal extent which can disrupt the near-wall regions, and impose a holistic modification on the boundary layer (Marusic *et al.* 2015; Buxton *et al.* 2018; Tang *et al.* 2024). This is very similar to the function of the very-large-scale structures in high-Re_τ TBLs in consideration of the 'footprints' and modulation effects by the large scales (Baars, Hutchins & Marusic 2017; Marusic, Baars & Hutchins*c* 2017). Importantly, it reveals that the artificially thickened boundary layer has the potential to simulate its canonical counterparts of high-Re_τ TBL flows. In fact, these over-tripped TBL flows widely exist in practical systems, which are stimulated by the effects of roughness, separation, pressure gradients, incoming turbulence, etc.

Notably, the artificially generated TBL flows are beyond canonical flows with the feature of significant changes throughout the boundary layer in all aspects of the mean flow, turbulence energy and scale interactions. However, the existence of self-similarity is less extensively explored under these non-canonical TBL conditions. A sound understanding of the scaling universality behaviour in artificially thickened conditions is essential for generalizing the self-similarity to more general flows. To explore the self-similarity behaviour of the artificially thickened TBL flows, two primary aspects should be considered. Firstly, the equilibrium between the inner layer and the wall is dramatically disrupted by the emergence of large-scale structures generated from over-tripped configurations (Marusic *et al*. 2015; Buxton *et al*. 2018; Tang *et al*. 2024). The inner region undergoes an adaptation process, gradually recovering from the tripping influence. This raises concerns about whether inner-layer self-similarity holds under non-canonical conditions. On the other hand, establishing self-similarity in the outer layer poses a significant challenge due to the dominance of energetic large-scale wake motions and their dependence on the tripping configurations. Moreover, these generated large-scale structures inherently differ from naturally developed very large-scale motions in canonical TBL flows. Consequently, the outer layer is intuitively assumed to lack universality. Therefore, given the above consideration, the current study aims to examine whether self-similar behaviour for the ECR scales is established in the inner region or if the outer-layer self-similarity can be observed in the impact of the external intermittency in the over-tripped conditions.

1.3. *Paper outline*

The objective of this paper is to study the effect of over-tripped configurations on the self-similarity of the TBL flows in the adaptation region, allowing for meaningful exploration of scaling universality behaviours in artificially thickened TBL flows. The analysis is based on the self-similarity of low-order and higher-order velocity structure functions, by mainly considering two factors: the popularity of the ECR scales in the inner region and the intrinsic scale-sensitive features of intermittency in the outer region. In the remainder of the paper, we introduce in § 2 the experimental dataset of the artificially thickened boundary-layer flows on which the analysis is based. In § 3, we systematically study structure functions at different orders of ECR scales under the tripping influence from the self-similarity perspective. The analysis is carried out in the inner region. On the other hand, the impact of external intermittency on the self-similarity of structure functions is discussed in § 4, and the self-similar behaviours within the ISR are further observed by conditional structure functions. A conclusion is given in § 5.

2. Experimental dataset description

A detailed description of this facility and flow conditions is provided by Tang *et al.* (2024). Specifications of experimental parameters and tripping configurations are given in table 1. Experiments were conducted in a closed-circuit wind tunnel in Tianjin University, as described in previous studies (Tang *et al.* 2016; Tang & Jiang 2020). The test section of the tunnel was 2.0 m long, 0.6 m tall and 0.8 m wide. A smooth boundary-layer plate was vertically fastened at the test section. The flat plate had a size of 1.75 m × 0.6 m × 0.015 m (length × width × thickness) with a 4 : 1 elliptical leading edge. In the current experiments, it had three different free-stream velocities of $U_\infty \approx 5.5$, 9.0 and 13.6 m s^{-1}. Transverse cylindrical rods of different diameters, $D_c = 1$, 2, 3, 4, 6, 8, 10, 12, 14, 17, 20 mm, were employed as the tripping devices, which were mounted at the position 80 mm downstream of the leading edge of the plate. The current trips have a wide range of $Re_D \approx 300-17\,000$ ($Re_D = U_\infty D_c / \nu$) which could have a considerable effect on the boundary layer at each free-stream velocity, as suggested in one of the pioneer works in this area by Erm & Joubert (1991). The cylindrical rods were made of ceramic zirconia materials with high hardness and toughness. The ceramic zirconia cylindrical rod was glued onto accurately machined metal inserts which were bolted into a recess and flush with the flat plate wall. The diameter of the tripping rods ($D_c = 1-20$ mm) was assumed to be the only parameter considered at each free-stream velocity. From the basic flow parameters shown in table 1, it can be seen that the boundary-layer flows tripped by the relatively small tripping diameters, such as the cases I-D2, II-D2 and III-D2, are very close to canonical TBLs. For case I-D1, the boundary layer is considered to be under-tripped at the measurement location, and will not be involved in the discussion of this study. Thus, these tripping configurations provide a comprehensive insight into the effect of the tripping rod diameters on the boundary-layer flows from moderate to over-stimulation.

In the experiment, the static wall pressure was measured through four pressure ports in the region $x = 0.78-1.58$ m downstream of the leading edge. The coefficient of pressure along the measurement positions was constant to within $\pm 0.82\,\%$ of the free-stream dynamic head for the moderately tripped cases, which is comparable in quality to related studies (Marusic *et al.* 2015; Sanmiguel Vila *et al.* 2017). The pressure deviation was also acceptable in all the over-tripped cases, which should be attributed to the large ratio between the distance from the flat plate to the tunnel ceiling and the maximum displacement thickness (which was below approximately 1.3 %). Hot-wire measurements

Case	D_c (mm)	U_∞ (m s^{-1})	Re_D	x_θ	Re_τ	Re_θ	δ (mm)	ν/u_τ (μm)	H	l^+	Δr^+	TU_∞/δ
I-D1	1	5.40	344	1362	81	333	6.9	82.1	2.18	15.2	0.11	83 173
I-D2	2	5.46	696	485	482	947	29.6	59.5	1.43	21.0	0.21	19 356
I-D3	3	5.52	1055	451	524	1028	32.0	59.2	1.42	21.1	0.22	18 060
I-D4	4	5.50	1401	436	525	1062	32.3	59.7	1.41	20.9	0.21	17 838
I-D6	6	5.58	2132	395	622	1188	37.8	58.9	1.39	21.2	0.22	15 450
I-D8	8	5.49	2797	346	796	1335	48.8	59.4	1.35	21.0	0.22	11 797
I-D10	10	5.61	3573	311	855	1515	51.6	57.8	1.33	21.6	0.23	21 062
I-D12	12	5.67	4334	296	1009	1612	59.8	57.4	1.31	21.8	0.23	19 843
I-D14	14	5.31	4735	261	1208	1714	76.3	61.2	1.29	20.4	0.20	14 591
I-D17	17	5.35	5793	280	1091	1606	68.1	60.4	1.30	20.7	0.21	16 457
I-D20	20	5.45	6943	254	1237	1803	76.3	59.8	1.28	20.9	0.21	14 983
II-D1	1	9.09	579	698	562	1094	21.0	36.1	1.40	34.6	0.23	18 182
II-D2	2	8.95	1140	533	688	1412	27.0	38.1	1.40	32.8	0.21	13 886
II-D3	3	8.98	1716	506	687	1490	27.0	38.1	1.39	32.8	0.21	13 909
II-D4	4	8.98	2288	490	757	1542	29.6	37.8	1.37	33.1	0.21	12 713
II-D6	6	8.95	3420	434	934	1732	36.6	38.0	1.35	32.9	0.21	20 511
II-D8	8	8.91	4540	385	1180	1945	46.1	37.8	1.32	33.0	0.21	16 215
II-D10	10	8.79	5599	345	1462	2140	56.9	37.7	1.29	33.2	0.21	12 964
II-D12	12	9.08	6940	303	1693	2514	65.3	37.4	1.27	33.4	0.22	11 652
II-D14	14	9.01	8034	281	1753	2691	68.1	37.6	1.26	33.2	0.21	11 094
II-D17	17	9.04	9789	292	1907	2606	73.6	37.4	1.26	33.5	0.22	10 311
II-D20	20	9.09	11 580	252	2253	3032	87.3	37.5	1.24	33.3	0.22	8739
III-D1	1	13.66	870	588	916	1952	24.3	25.7	1.37	47.2	0.22	23 594
III-D2	2	13.49	1718	574	898	1976	24.3	26.2	1.37	46.3	0.21	23 301
III-D3	3	13.54	2587	544	1007	2091	27.0	26.0	1.36	46.5	0.22	20 989
III-D4	4	13.76	3506	523	1121	2213	29.6	25.6	1.35	47.3	0.23	19 499
III-D6	6	13.65	5217	466	1322	2465	35.1	25.7	1.32	47.1	0.22	16 321
III-D8	8	13.53	6894	385	1833	2952	48.8	25.8	1.28	46.9	0.22	11 619
III-D10	10	13.46	8573	327	2342	3460	62.6	25.9	1.25	46.8	0.44	18 044
III-D12	12	13.75	10 510	287	2674	4023	70.8	25.6	1.24	47.2	0.45	16 283
III-D14	14	13.46	12 003	278	2821	4077	76.3	26.2	1.24	46.2	0.43	14 794
III-D17	17	13.68	14 813	297	2786	3871	73.6	25.6	1.24	47.3	0.45	15 595
III-D20	20	13.72	17 478	240	3546	4813	95.0	25.9	1.22	46.6	0.44	12 106

Table 1. Experimental parameters for the profiles of different tripping conditions at different free-stream speeds.

were carried out at the streamwise location $x = 1.32$ m downstream of the trip. The location in dimensionless form $x_\theta = x/\theta$ (θ is the momentum thickness of boundary layer) is shown in table 1. The streamwise location is located at the adaptive region in the over-tripped conditions, which as expected supplies the data for the examination of the self-similarity in artificially thickened TBL flows. Boundary layer traverses were conducted by a miniature single-sensor boundary-layer probe (TSI-1621A-T1.5). The probe was used with a constant temperature anemometer system of IFA-300 operating at an overheat ratio of 1.7. The tungsten (platinum-coated) hot-wire has a sensitive length of 1.25 mm and a diameter of 4 μm, resulting in a length-to-diameter ratio (l/d) of more than 200 (Ligrani & Bradshaw 1987; Hutchins *et al.* 2009). In terms of spatial resolution, the viscous-scaled wire length (l^+) is less than $l^+ < 48$ for all the measurement cases. Following the suggestions of negligible energy content by Hutchins *et al.* (2009), the sampling frequency was set up and the corresponding non-dimensional sample interval was $\Delta t^+ < 0.5$ ($\Delta t^+ = \Delta t u_\tau^2/\nu$, where $\Delta t = 1/f$, f is the sampling frequency and u_τ is the friction velocity). Note that the current sampling frequency is higher than the effective frequency that can be resolved by the current hot-wire probe of $l^+ \to 48$. The total sampling time at each wall-normal location is given by T, which is normalized in outer variables to give boundary-layer turnover times TU_∞/δ (in table 1). For converged statistics, these numbers need to be large, since the largest structures in high-Re_τ TBLs can exceed 20δ (Kim & Adrian 1999; Guala, Hommema & Adrian 2006; Hutchins & Marusic 2007*b*), and we would typically require several hundreds of these events to flow past the hot-wire sensor before we could expect converged statistics. In this study, the total sampling time was set in such a way that the boundary-layer turnover time was in the range of 8500–23 500 for all the measurements. Due to the limit on the amount of memory, the sampling time in each case was changed with the given sampling frequency to make sure that there were more than 8 500 boundary-layer turnover times for all the measurements, which adequately covers the energy contained in the largest scales (Hutchins *et al.* 2009; Mathis, Hutchins & Marusic 2009) and acquires converged statistics. Calibration was employed by Air Velocity Calibrator Model 1127 of IFA-300 over a velocity range of 0 to 22 m s^{-1}. The hot-wire probe was translated to all the wall-normal positions in the experiments by using a computer-controlled translation stage. The number of wall-normal measurement stations with logarithmical spacing was increased as the boundary-layer thickness increased. In addition, the adjustment of the wall-normal offset of the probe sensor was monitored by a digital microscope-based procedure.

Inner-normalized mean streamwise velocity profiles, $\langle U \rangle^+$ versus y^+, are shown in figure 1 for all the tripping conditions at different free-stream velocities. Considering the strong impact of the tripping configurations on the mean flow fields, the friction velocity, u_τ, is estimated from the raw mean velocity by fitting a composite profile by Rodríguez-López, Bruce & Buxton (2015). As shown, the mean velocity profiles for different tripping diameters collapse in the near-wall region. For comparison, the inner velocity profile of Musker (1979) is superimposed as a black line, in which the von Kármán constant $\kappa = 0.41$ and the constant $B = 4.86$ (Nagib & Chauhan 2008; Marusic *et al.* 2013; Segalini, Örlü & Alfredsson 2013). The agreement also suggests that the near-wall region is more prone to adapting quickly to a canonical TBL under the tripping impact, which is similar to the previous investigations (Schlatter & Örlü 2012; Rodríguez-López, Bruce & Buxton 2016*a*; Rodríguez-López *et al.* 2017*b*). On the contrary, a significant difference is observed in the outer layer, showing a progressively repressive wake region with increasing D_c. Similar to the TBLs stimulated by other kinds of tripping conditions (Marusic *et al.* 2015; Dogan, Hanson & Ganapathisubramani 2016), the current over-tripped effects could
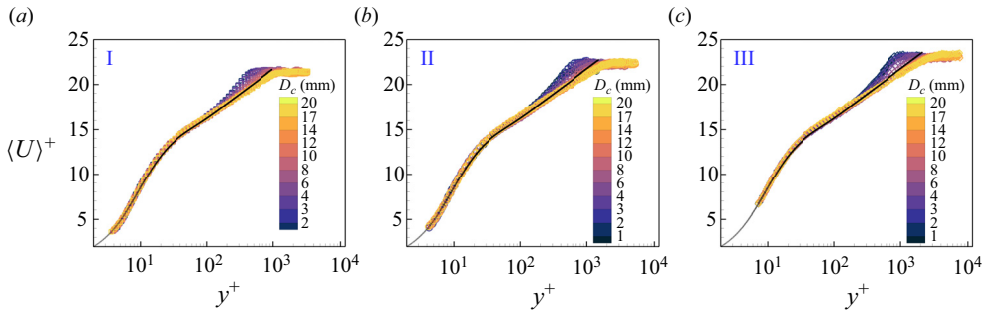
Figure 1. Inner-normalized mean velocity profiles for the different D_c at different free-stream speeds: (*a*) case I, (*b*) case II and (*c*) case III. The solid black lines show the Musker profile (Musker 1979) with constants $\kappa = 0.41$ and $B = 4.86$.
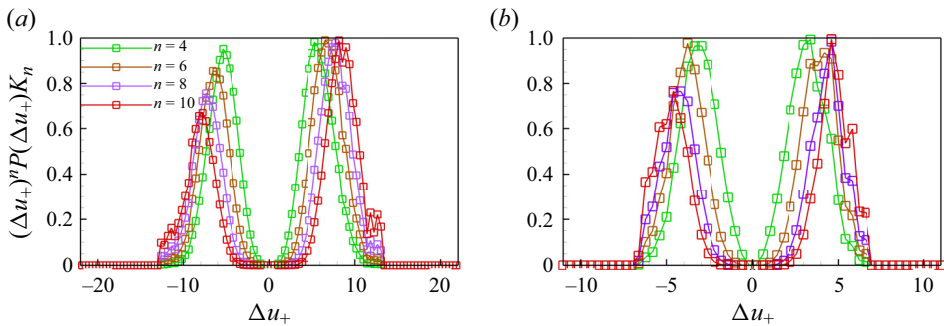

Figure 2. Pre-multiplied p.d.f. of $(\Delta u_+)^n P(\Delta u_+)$ at two representative wall-normal heights in the inner and outer region for case III-D20: (*a*) at $y^+ \approx 80$ and (*b*) at $y/\delta \approx 0.87$, with the spatial distance $r \approx \delta$. Curves are multiplied by an arbitrary factor K_n to get the normalized maximum for all orders.

result in a suppression of the wake region by introducing the generated wake flows, which leads to lower velocity in the modified region, as shown in figure 1.

Prior to calculating the higher-order moments of the streamwise structure function, it is necessary to inspect the statistical convergence of the higher moments, which can be verified by examining the pre-multiplied probability density function (p.d.f.) of velocity increments, $(\Delta u_+)^n P(\Delta u_+)$, following the approach used in previous works (Meneveau & Marusic 2013; Yang, Marusic & Meneveau 2016*a*; de Silva *et al.* 2017). Figure 2 plots the results for case III-D20 at two representative wall-normal heights in the inner and outer regions. For the inner region, the reference location is at $y^+ \approx 80$, and the other reference location is at $y/\delta \approx 0.87$, corresponding to an intermittency parameter of $\gamma(y) \approx 0.55$ (γ represents the proportion of time that the hot-wire probe records turbulent fluids). It can be noted that an acceptable convergence degree of the current dataset is up to $n = 8$. The results show acceptable 'closure' of the pre-multiplied p.d.f. with the smooth tails in the sense that the structure function, which is the area under the curve, is well captured. However, convergence at the order of $n = 10$ is moderate, therefore, for the current analysis results at the order of $n > 8$ should be considered with due caution. Similar convergence results are obtained for the other data used in the current study.
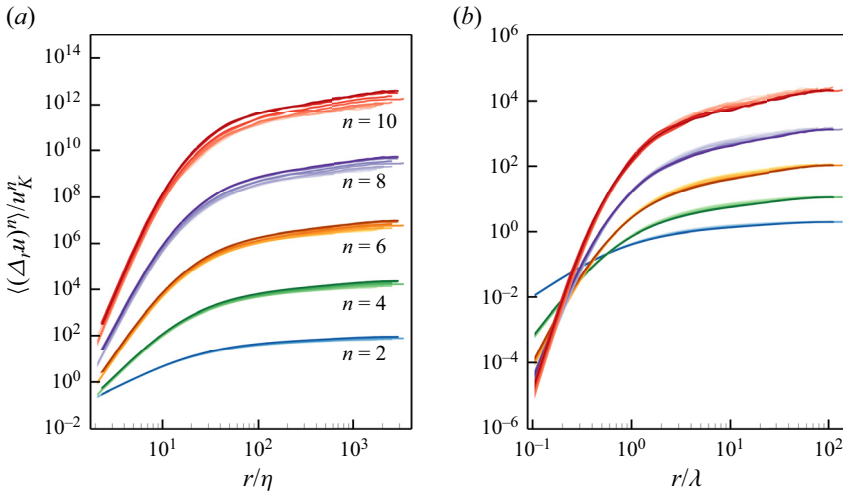
984 A34-8

Figure 3. Distribution of even-order structure functions up to the tenth order at $y^+ \approx 80$ for various tripping conditions with different rod diameters in case III. The structure functions are normalized by (*a*) the Kolmogorov scales and (*b*) the Taylor scales. The line colour from light to dark corresponds to increasing tripping rod diameters from $D_c = 1$ to 20 mm in case III.

3. Self-similarity in the inner region of over-tripped boundary layers

3.1. *Structure functions in the inner region*

To explore the self-similarity of structure functions in the inner region under the impact of the over-tripped conditions, the even-order structure functions up to the tenth order are plotted in figure 3. The structure functions are normalized by the different characteristic scales, which are the Kolmogorov scales (Kolmogorov velocity $u_K = (\nu\langle\varepsilon\rangle)^{1/4}$ and Kolmogorov length $\eta = (\nu^3/\langle\varepsilon\rangle)^{1/4}$, where $\langle\varepsilon\rangle = 15\nu(\partial u/\partial x)^2$ is the estimate of the mean dissipation rate based on the local-homogeneity assumption) and the Taylor scales (the root mean square of the velocity fluctuations $u_\lambda = \langle u^2\rangle^{1/2}$ and Taylor length scale $\lambda = (15\nu u_\lambda^2/\langle\varepsilon\rangle)^{1/2}$). In figure 3, the line colour for each order structure function switching from dark to light represents an increase of the rod diameter from $D_c = 1$ to 20 mm in case III. In the plot, the higher-order structure functions are presented since they hold the information about internal intermittency (Landau & Lifshitz 1963), which represents a stochastic behaviour of very intense fluctuations with a higher frequency of occurrence than that predicted by a Gaussian distribution and occurs predominantly at the small scales. In the current study, with increasing tripping rod diameter, the large-scale structures generated by the tripping configurations are enhanced, which provides a modification effect on the small scales in the inner region (Mathis *et al.* 2009; Baars *et al.* 2017; Marusic *et al.* 2017; Tang *et al.* 2024). Thus, under the tripping influence in the over-tripped conditions, whether the similarity of the ISR could be established arouses our interest.

Figure 3 shows the even-order structure functions at the wall-normal location of $y^+ \approx$ 80. In figure 3(*a*), for the second order, there is reasonable support for self-similarity for various tripping configurations, since an adequate collapse of structure functions can be observed almost over the entire *r* space. At the smallest scales, the collapse is perfect, which suggests the structure functions obey the classical Kolmogorov scaling $\langle(\Delta_r u)^2\rangle/u_K^2 \propto (r/\eta)^2$. At the largest scales, the self-similarity still holds with acceptable accuracy despite the tripping influence and finite-Reynolds-number effects. However, the

situation is different for the higher-order structure functions. The self-similarity of structure functions is not strictly valid. Specifically, the eighth- and tenth-order structure functions normalized by the Kolmogorov scales (u_K and η) reveal a non-collapsing and clearly non-self-similar arrangement over the entire range of scales. In addition, as regards the performance of the Kolmogorov similarity at the smallest scales, it requires higher-resolution datasets for observation. Similarly, the structure functions do not satisfy the self-similarity over the entire scale range after normalization with the Taylor scales (figure 3*b*). As shown, except for the collapse at the intermediate scales, the Taylor scales lead to a certain discrepancy in the dissipative range and at the large scales on increasing the order. This finding confirms the general understanding of turbulence that the structure functions do not feature universality over the entire range of scales, specifically at low to moderate Reynolds numbers (Pearson & Antonia 2001).

As indicated in the previous investigation (Landau & Lifshitz 1963), the non-universality of the higher-order structure functions is highly sensitive to different effects, such as internal intermittency and finite-Reynolds-number effects. Especially, in the current study, the generated large-scale wake structures by the over-tripped rods have amplitude and frequency modification effects on the small scales in the inner region, as presented in Appendix A. Both the amplitude and frequency modulation coefficients are increased with the tripping diameter, which means that generated large-scale structures could alter the internal intermittency behaviour based on modulation effects and result in the non-universality of the higher-order statistics, as shown in figure 3.

Figure 4 plots the comparison of the p.d.f.s of the velocity gradients $\partial u/\partial x$ at the wall-normal height $y^+ \approx 80$ for various tripping cases III-D1–D20. It shows that the p.d.f.s are non-Gaussian and have stretched exponential tails, which is very similar to the p.d.f.s in many other kinds of turbulent flows, such as isotropic turbulence (Gotoh, Fukayama & Nakano 2002) and turbulent jet flows (Gauding *et al.* 2021). On increasing the tripping rod diameter, the p.d.f.s have almost a consistent distribution. Careful observation shows that the tails of the p.d.f.s become slightly stretched in the over-tripped cases, which should be related to the footprint of large-scale wake structures generated by the tripping condition with increasing rod diameter (the evidence of the footprint effect of large scales in the near-wall region is exhibited in Appendix B).

3.2. *Relative relations of structure functions for the ECR scales*

In the spirit of the ESS hypothesis, the relation of the velocity structure functions as expressed in (1.4) for the ECR scales is examined to further explore universality in this part. Following the previous work from de Silva *et al.* (2017), figure 5 plots the relation of $\langle (\Delta_r u_+)^{2p} \rangle^{1/p}$ versus $\langle (\Delta_r u_+)^2 \rangle$ at $y^+ \approx 80$ for all the cases III-D1–D20. All the results are computed at a fixed wall-normal location of $y^+ \approx 80$, similar to that processed in figures 3 and 4. In the plot, the tenth-order ($2p = 10$) structure function is also involved to highlight any subtle differences in the ESS framework. In figure 5, the distributions of $\langle (\Delta_r u_+)^{2p} \rangle^{1/p}$ versus $\langle (\Delta_r u_+)^2 \rangle$ for almost all the scales are shown by the coloured lines, from which the ESS scaling cannot be extracted directly, as shown by de Silva *et al.* (2017). However, for the ECR-scale range of $y < r < \delta$, as marked by the symbols, the results obviously reveal a convincingly extended range of scaling behaviour in the ESS-inspired framework. The results show a good collapse of the higher-order moments up to $2p = 10$ and provide direct support for the investigation of de Silva *et al.* (2017). Furthermore, the current study extends the application of the ECR-scale similarity to the over-stimulated boundary layers, which are in an adaptation region to recover from the
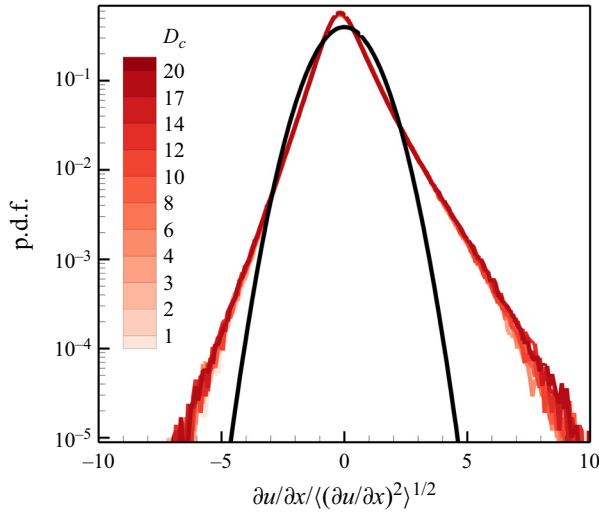
Figure 4. Comparison of p.d.f.s of velocity gradients at $y^+ \approx 80$ for various tripping conditions with different rod diameters in cases III-D1–D20. The black dashed line indicates a normal distribution. The curves are normalized by the standard deviation $\langle (\partial u/\partial x)^2 \rangle^{1/2}$.
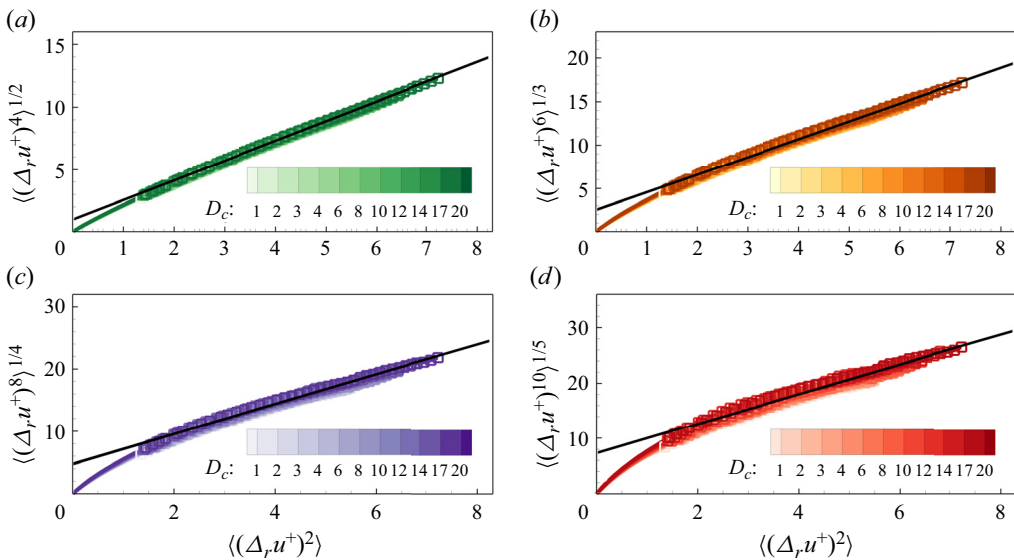

Figure 5. The ESS plot for higher-order moments for the same databases shown in figures 3 and 4. The results are computed at the wall-normal location of $y^+ \approx 80$; $\langle (\Delta_r u_+)^{2p} \rangle^{1/p}$ versus $\langle (\Delta_r u_+)^2 \rangle$: (a) $p = 2$, (b) $p = 3$, (c) $p = 4$, (d) $p = 5$, as shown in the coloured lines for almost the entire scale range of r. The data in the ECR-scale range of $y < r < \delta$ are shown by the symbols. The solid black lines (——) correspond to a fit following (1.4) in the ECR-scale range at case III-D20.

leading-edge tripping effects and return to the canonical state. The good agreement for each higher order $2p = 4, 6, 8, 10$ in figure 5 suggests that the scaling behaviour of ECR scales is independent of the current tripping influence.

The extended range of scaling behaviour in figure 5 provides an opportunity to have a reliable estimation of the scaling coefficients (slopes $D_p/D_1, p = 2, 3, 4, 5$). To further
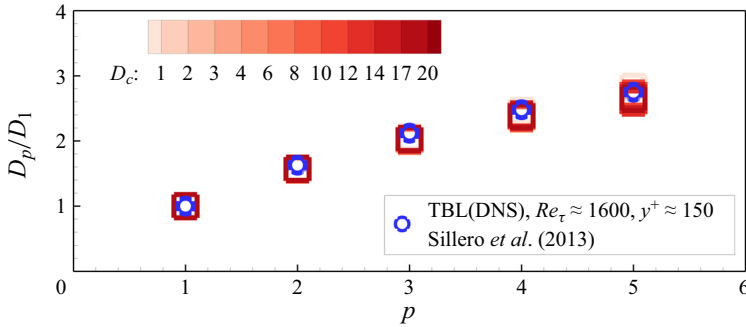
Figure 6. Distribution of ratios D_p/D_1 versus p, from the relation in figure 5. The symbol of the blue circle represents the results of TBL DNS datasets ($y^+ \approx 150$, $Re_\tau \approx 1600$) from Sillero *et al.* (2013).

quantify the relation, the ratios of D_p/D_1 are computed based on a linear fit in the ECR-scale range $y < r < \delta$. The work of de Silva *et al.* (2017) utilized this procedure to exhibit a good description of the ECR-scale similarity at $Re_\tau \approx 900$, which indicates that ECR scaling coefficients can be confidently estimated from databases at low Reynolds numbers when no clear logarithmic region exists. The current study confirms the scaling universality of ECR scales based on the datasets in the range of $Re_\tau \approx 500-3500$, especially under the tripping influence. Figure 6 shows the estimates of the higher-order slope ratios D_p/D_1 over a range of ECR scales for various tripping rods with different diameters. We can note that the coefficient ratio D_p/D_1 holds a consistent distribution for all the tripping cases. For comparison, the results in the inner region of TBL flow ($y^+ \approx 150$, $Re_\tau \approx 1600$) by Sillero, Jiménez & Moser (2013) are also shown in the plot. As shown, D_p/D_1 in the current study is in accordance with the result by Sillero *et al.* (2013). The consistent scaling behaviour confirms that the relation of the structure functions in the ECR scales is independent of the different tripping conditions in the current study.

Furthermore, to explore the performance of the structure functions for the ECR scales at a broader wall-normal extent, figure 7 plots the distribution of ratios $D_p/D_1 (p = 2, 3, 4, 5)$ across the entire boundary layer for all the tripping cases. Similar to figure 6, the coefficient ratio calculated from the direct numerical simulation (DNS) TBL datasets by Sillero *et al.* (2013) ($y^+ \approx 150$, $Re_\tau \approx 1600$) is employed for comparison (black lines). As shown, a good collapse of the ratio is noted in the inner region for the various tripping conditions, which indicates that the scaling universality of the ECR scales is independent of the tripping rod diameter. Meanwhile, the values of D_p/D_1 in the inner region appear unchanged. This constant of D_p/D_1 is consistent with the suggestions by de Silva *et al.* (2017) in the log region of high-Reynolds-number TBLs. In addition, based on the ESS-inspired framework, the universality of the scaling of the ECR scales extends beyond the logarithmic region of the boundary layer. From the insets in figure 7, it can be seen that the universality extends almost up to $y/\delta \approx 0.5$ for all the tripping cases. Since the boundary-layer thickness is increased with the tripping diameter, it can be deduced that a further reaching universality is performed by increasing the tripping rod diameter.

From these findings, it can be concluded that, even though the tripping impacts are likely to be embodied in structure functions at different orders, as shown in figures 3 and 4, we are able to exhibit the similarity of ECR scales by accurately quantifying the universal scaling of the ratios between two structure functions (D_p/D_1) over a much larger wall-normal extent. Analogously, recent work on high-order moments (Yang *et al.* 2016*a*,*b*; Xia *et al.*
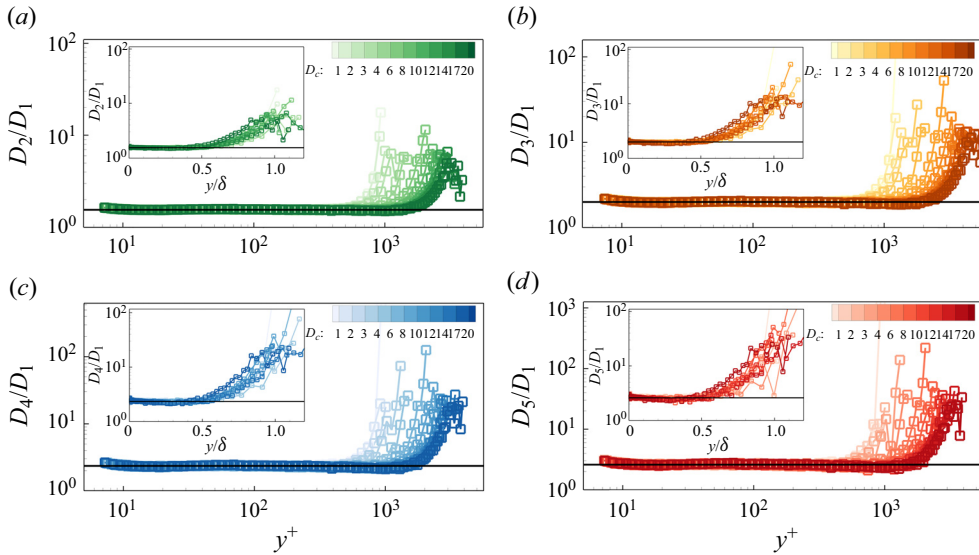
Figure 7. Distribution of ratios D_p/D_1 along the wall-normal heights of y^+ (y/δ in the insets) for all the tripping cases III-D1–D20; (*a*) $p = 2$, (*b*) $p = 3$, (*c*) $p = 4$ and (*d*) $p = 5$. The coefficient ratio value calculated from the TBL DNS datasets ($z^+ \approx 150$, $Re_\tau \approx 1600$) from Sillero *et al.* (2013) is also plotted in black lines for comparison. The results of ratios D_p/D_1 for cases I and II are shown in Appendix C.

2018) also indicated that the extent of logarithmic scaling as a function of *y* increases when examining ratios between moment functions in ESS form. The observation of the ESS region could be attributed to the argument that the bulk flow or viscous effects have a similar action on the structure function for the ECR scales (Yang *et al.* 2016*a*,*b*), which can be further extended under the over-tripped conditions.

Additionally, the relative relation of structure functions in (1.4) is challenged in the outer part around the edge of the boundary layer. This region is dominated by the turbulent/non-turbulent intermittency, rather than the ECR scales following Townsend's attached hypothesis. Hence, it is reasonable to note an obvious discrepancy in the examination of the scaling for ECR scales in the ESS framework, as shown in figure 7. In the following, the similarity behaviour in the outer region will be examined by considering the external intermittency.

4. Self-similarity in the outer region with external intermittency

In this section, we examine whether structure functions in the outer region admit self-similarity under the influence of the tripping condition and discuss the effects of external intermittency.

4.1. *The external intermittency*

The external intermittency is described as the flow alternating between turbulent and substantially irrotational non-turbulent motions in the outer-layer region (Corrsin & Kistler 1955; Townsend 1976). The turbulent region and non-turbulent region are separated by the turbulent/non-turbulent interface (TNTI), which is assumed to be a sharp and highly contorted superlayer (Bisset, Hunt & Rogers 2002; Chauhan *et al.* 2014; da Silva *et al.* 2014; Philip *et al.* 2014). The mean intermittency distribution is argued to be independent of Reynolds number (Fiedler & Head 1966). In the artificially thickened

boundary-layer flows, the generated wake structures from the leading-edge trips can provide a remarkable alteration to the external intermittency in the adaptive region (Rodríguez-López *et al.* 2016*a*; Buxton *et al.* 2018; Tang *et al.* 2024), by inquiring into the statistics of the outer-layer region, such as mean velocity, variance, energy spectra and high-order statistics.

To observe the external intermittency behaviour, it is necessary to detect the TNTI, which is a continuous ongoing research activity in turbulent flows. Several detecting methods have also been proposed for the experimental datasets, by considering that the intrinsic background turbulence in free stream. For particle image velocimetry measurements, the TNTI was detected by the technique based on turbulent kinetic energy (Chauhan *et al.* 2014), local homogeneity (Reuther & Kähler 2018), fuzzy clustering of the streamwise velocity field (Fan *et al.* 2019; Younes *et al.* 2021), track of the Lagrangian particle trajectories (Long, Wu & Wang 2021) and so on. For the current one-dimensional flow data by hot-wire measurement, the detection of intermittency relies upon identifying whether the probe is measuring turbulent or non-turbulent fluids. Therefore, a turbulent kinematic energy criterion proposed by Chauhan *et al.* (2014) is utilized to detect the TNTI in this study. This procedure has been extensively used in recent works (de Silva *et al.* 2013; Chauhan *et al.* 2014; Kwon, Hutchins & Monty 2016; Saxton-Fox & McKeon 2017; Buxton *et al.* 2018; Chen *et al.* 2023), and only a brief description will be given here.

The intermittency interface detector function is introduced to evaluate the external intermittency, which is defined as

$$\varphi(i) = \frac{100}{U_\infty^2} \frac{1}{3} \sum_{j=-1}^{1} (u_{i+j} - U_\infty)^2, \tag{4.1}$$

where the index i is an arbitrary instant in the temporal domain and the summation over index j indicates a mean over three consecutive measurements in a time series. The turbulent (non-turbulent) fluids can be detected as those for which $\varphi(i)$ is higher (lower) than a given threshold φ_{th}. A binary representation of the flow is obtained using the threshold, and the binary representation is considered as

$$\psi(i) = H(\varphi(i) - \varphi_{th}) = \begin{cases} 1, & \varphi(i) \geq \varphi_{th} \\ 0, & \varphi(i) < \varphi_{th} \end{cases}, \tag{4.2}$$

where H is the Heaviside function and $\psi(i)$ is the so-called intermittency function. Then, as proposed by Klebanoff (1955), an intermittency parameter $\gamma(y)$ at the wall-normal location of y is defined as

$$\gamma(y) = \frac{1}{N} \sum_{i=1}^{N} \psi(i, y), \tag{4.3}$$

which quantifies the proportion of time that the flow is turbulent. Close to the wall, the flow is expected to be fully turbulent, $\gamma(y) = 1$, the non-turbulent fluids gradually have more occurrence far away from the wall, and $\gamma(y) = 0$ in the free stream. It is well known that the intermittency profile of $\gamma(y)$ in the TBL can be described by the error function (Corrsin & Kistler 1955; Klebanoff 1955; Fiedler & Head 1966; Hedleyt & Keffer 1974)

$$\gamma(y) = \frac{1}{\sigma_I \sqrt{2\pi}} \int_y^\infty \exp\left(-\frac{(y - Y_I)^2}{2\sigma_I^2}\right) dy, \tag{4.4}$$
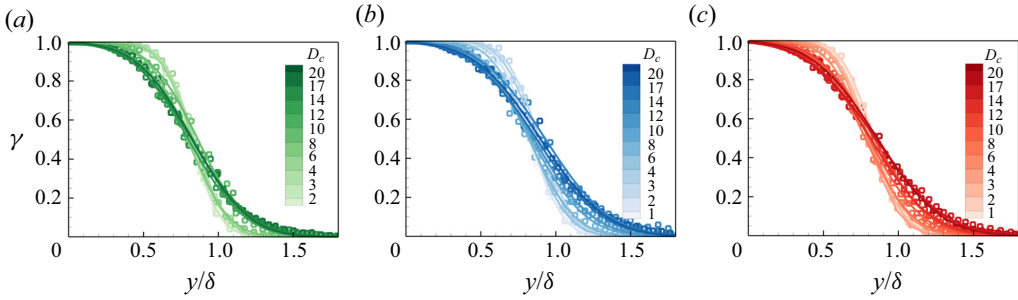
Figure 8. Intermittency parameter profile $\gamma(y)$ as a function of y/δ in outer scaling for different tripping rod diameters with different free-stream velocities; (*a*) case I, (*b*) case II, (*c*) case III. Coloured lines represent the result by fitting (y) to the error function in (4.4).

here, Y_I is the wall-normal location of the mean interface where $\gamma(Y_I) = 0.5$ and σ_I is the standard deviation of the instantaneous interface position y_I relative to the mean position Y_I. Here, Y_I and σ_I are the estimated parameters by fitting the measurement intermittency profile to the function of (4.4). From the above procedure, it can be seen that the intermittency is dependent on the given threshold value φ_{th}, which is related to the values of Y_I and σ_I. Thus, by fitting the error function in (4.4), a threshold of 0.07–0.08 is chosen to calculate the intermittency profile $\gamma(y)$ for all the cases in the current study. The wall-normal intermittency profiles $\gamma(y)$ in the outer scaling y/δ are shown in figure 8. As shown, $\gamma(y)$ exhibits a normal distribution for all the tripping conditions in the current study, by presenting good fittings to the error function in (4.4). Considering that the current tripping conditions make a significant alteration to the flow fields in the wake region, this could challenge the fit precision based on the wake function in determining the 'true' boundary-layer thickness (the wall distance where $\bar{U} = U_\infty$ exactly) (Chauhan *et al.* 2009). Thus, the conventional boundary-layer thickness ($y = \delta$ where $\bar{U}/U_\infty = 0.99$) is used in this study, which is smaller than the 'true' boundary-layer thickness (Chauhan *et al.* 2009). As shown in figure 8, $\gamma \approx 0.2-0.4$ (increase with D_c) at $y/\delta = 1$ in all cases, which is consistent with the previous investigations (Kovasznay, Kibens & Blackwelder 1970; Hedleyt & Keffer 1974; Chen & Blackwelder 1978; Chauhan *et al.* 2014). The standard deviation σ_γ of the interface location is presented as a function of the tripping rod diameter in figure 9. The solid line indicates the range of $\sigma_\gamma \approx 0.15-0.18$, which is obtained from the data of canonical TBL flows (Corrsin & Kistler 1955; Hedleyt & Keffer 1974). It shows that σ_γ has a good agreement with the results in the moderately tripped cases. Then, increasing D_c alters the intermittent region by introducing strong perturbations. The intermittency region rapidly extends further away from the wall by holding a wider proportion in the boundary layer, as shown in figure 8, thus, an increased σ_γ is noted in figure 9.

With this definition of the intermittency parameter γ, any conventionally averaged quantity $\langle\phi\rangle$ can be decomposed as

$$\langle\phi\rangle = \gamma\langle\phi\rangle_T + (1-\gamma)\langle\phi\rangle_N, \qquad (4.5)$$

where $\langle\phi\rangle_T$ and $\langle\phi\rangle_N$ indicate the conditional averaging results by only considering either turbulent or non-turbulent regimes (Mellado, Wang & Peters 2009; Gauding *et al.* 2021). The conditional averages are defined with the binary indicator function, ψ, as

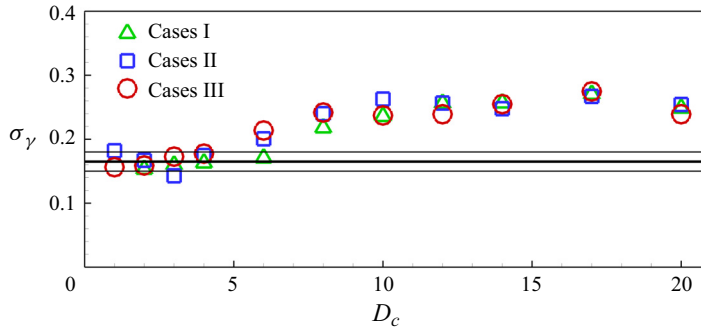$$\langle\phi\rangle_T = \langle\psi\phi\rangle, \qquad (4.6)$$

984 A34-15

Figure 9. Standard deviation of the interface location σ_γ as a function of tripping rod diameter D_c for the cases I, II and III. Solid line represents the range of $\sigma_\gamma \approx 0.15-0.18$.

and

$$\langle \phi \rangle_N = \langle (1 - \psi)\phi \rangle. \tag{4.7}$$

4.2. *Intermittency structure function*

Referring to the external intermittency, when we calculate the statistical moments of the velocity increments of two points separated by a spatial distance r, different conditions should be considered: (I) both points are located within the turbulent regime, (II) both points are within the non-turbulent regime and (III) one point in the turbulent regime and the other one in the non-turbulent regime. For locally homogeneous turbulence, the corresponding probabilities for the different conditions can be obtained as $\gamma_{TT} = \gamma - \frac{1}{2}\Theta_I$, $\gamma_{NN} = 1 - \gamma - \frac{1}{2}\Theta_I$ and $\gamma_{TN} = \Theta_I$, where $\Theta_I = \langle (\psi(x+r) - \psi(x))^2 \rangle$ is known as the intermittency structure function (Kuznetsov, Praskovsky & Sabelnikov 1992). It is clear that $\gamma_{TT} + \gamma_{NN} + \gamma_{TN} = 1$. From the probabilities in different conditions, it can be deduced that the ratio

$$\frac{\gamma_{TT}}{\gamma} = 1 - \frac{\Theta_I}{\gamma}, \tag{4.8}$$

which represents the conditional probability that one point of the velocity increment is in the turbulent regime considering that the other point is also in the turbulent regime. From the above equations, it can be deduced that $\gamma_{TT}/\gamma \to 1$ ($\gamma_{TT} \to \gamma$) as $\Theta_I \to 0$ if $r \to 0$. Figure 10 shows γ_{TT}/γ against spatial distance r/η at different wall-normal positions the intermittency of which is in the range of $\gamma = 0.1-0.9$ for case III-D20 as a representative case. It is expected that in the inner region with the higher value $\gamma \to 0.9$, γ_{TT}/γ is close to unity with $r \to 0$ and has a relatively slowly decreasing trend with increasing separation distance r. Further away from the wall, γ_{TT}/γ decreases remarkably at larger r. A similar distribution was reported in the turbulent jet flow by Gauding *et al.* (2021). Due to the external intermittency of the alternation between turbulent and non-turbulent fluid and the decreased proportion of turbulent excursion, it is reasonable to have lower γ_{TT}/γ toward the edge of the boundary layer ($\gamma \to 0.1$) at the larger-separation distance.

To further explore the feature of the intermittency function ψ, one-dimensional random telegraphic signals ψ_{ts} are introduced, which have randomly distributed values of $\psi_{ts} = 1$ in turbulent regimes and $\psi_{ts} = 0$ in non-turbulent regimes, with the corresponding probabilities of $P(\psi_{ts} = 1) = \gamma_{ts}$ and $P(\psi_{ts} = 0) = 1 - \gamma_{ts}$. The second-order moment of
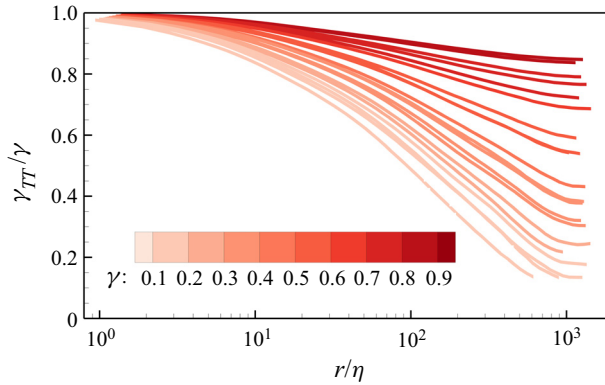
984 A34-16

Figure 10. Conditional probability γ_{TT}/γ against spatial distance, r/η, at different wall-normal positions with the intermittency parameter in the range of $\gamma = 0.1-0.9$ for case III-D20.

the increment $\Theta_{I,ts}(r)$ can be expressed by the autocorrelation function of ψ_{ts}, as

$$\Theta_{I,ts}(r) = \langle(\psi_{ts}(x+r) - \psi_{ts}(x))^2\rangle = 2(R_{\psi_{ts}}(0) - R_{\psi_{ts}}(r)) = 2(\gamma_{ts} - R_{\psi_{ts}}), \qquad (4.9)$$

where $R_{\psi_{ts}}(r)$ represents the analytical expression of the autocorrelation of ψ_{ts}, which is expressed as (Machlup 1954; Fitzhugh 1983; Thiesset *et al.* 2020)

$$R_{\psi_{ts}}(r) = \langle\psi_{ts}(x+r)\psi_{ts}(x)\rangle = \gamma_{ts}(\gamma_{ts} + (1 - \gamma_{ts})\,\mathrm{e}^{-r/\mathcal{L}_{ts}}). \qquad (4.10)$$

In (4.10), $\mathcal{L}_{ts}$ is a characteristic length scale, $\mathcal{L}_{ts} = 2\gamma_{ts}(1 - \gamma_{ts})[\lim_{r\to0}(\Theta_{I,ts}(r)/r)]^{-1}$, that relates to the probability of ψ_{ts} transiting from a value of 1 to 0 and *vice versa* (Machlup 1954; Fitzhugh 1983; Thiesset *et al.* 2020).

From the expression of (4.9) and (4.10), an analytical intermittency structure function of the random telegraphic signal can be expressed as

$$\Theta_{I,ts}(r) = 2\gamma_{ts}(1 - \gamma_{ts})(1 - \mathrm{e}^{-r/\mathcal{L}_{ts}}). \qquad (4.11)$$

From (4.11), it can be seen that, at large separations, $\Theta_{I,ts}(r \to \infty) = 2\gamma_{ts}(1 - \gamma_{ts})$, and for the small-separation limit it can be deduced that

$$\lim_{r\to0}\Theta_{I,ts}(r) = 2\gamma_{ts}(1 - \gamma_{ts})\frac{r}{\mathcal{L}_{ts}} + \mathrm{O}(r^2), \qquad (4.12)$$

which indicates that $\Theta_{I,ts}(r)$ is proportional to r when the separation distance r is small compared with $\mathcal{L}_{ts}$.

Then, we can compare the analytical intermittency structure function of the random telegraphic signal, $\Theta_{I,ts}$, with the intermittency structure function Θ_I of the wall turbulence signals for case III-20 in the current study. In figure 11, the intermittency structure function Θ_I is presented for the different wall-normal positions, which is normalized by the large-scale limit $2\gamma(1 - \gamma)$. The separation distance r is normalized by the characteristic length scale $\mathcal{L}$. The plot shows a good collapse between $\Theta_{I,ts}/2\gamma_{ts}(1 - \gamma_{ts})$ and $\Theta_I/2\gamma(1 - \gamma)$ at the scales of the small- and large-scale limits. A clear discrepancy is noted in the intermediate-scale range, which becomes more obvious as increasing wall-normal heights (decreasing intermittency parameter γ). This discrepancy was also reported in the intermittent range scales of turbulent jet flows (Gauding *et al.* 2021) and liquid–gas turbulence (Thiesset *et al.* 2020). In fact, the TNTI is widely argued
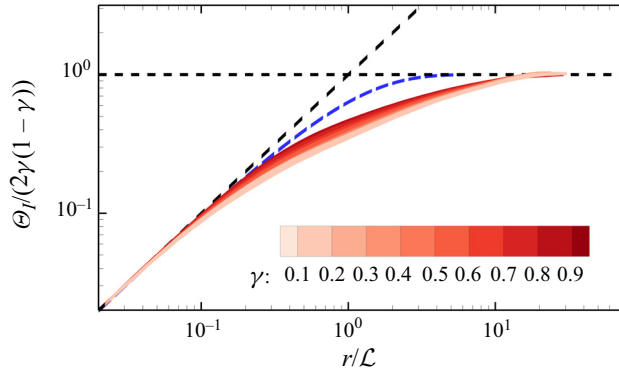
Figure 11. Comparison of the intermittency structure function Θ_I (coloured lines) at different wall-normal positions ($\gamma = 0.1-0.9$) with the analytical intermittency structure function of the random telegraphic signal ($\Theta_{I,ts}$, blue dashed lines). The black dashed lines indicate the analytical small- and large-scale limits. Data for case III-D20.

to be a self-similar fractal which can be quantified by the fractal dimension (Sreenivasan & Meneveau 1986). The self-similar fractal behaviour has been confirmed in different classes of flows, such as boundary layer, jet flow, plane wake and mixing layer (Sreenivasan & Meneveau 1986; Meneveau & Sreenivasan 1991). Furthermore, Tang *et al.* (2024) confirmed that, under the impact of the tripping conditions in the current study, the boundary-layer flows remain self-similar fractals with identical fractal dimensions. Thus, the discrepancy in the intermediate-scale range in figure 11 is due to the fact that the morphology of the TNTI is not fully random but instead characterized by the self-similar fractal behaviour of turbulence.

As mentioned earlier, the characteristic length scale $\mathcal{L}$ relates to the transiting probability of ψ, which is equivalent to the jump frequency transiting from a value of 1 to 0 and *vice versa*. The jump frequency is expressed as

$$f_\psi = \left\langle \left| \frac{\partial \psi}{\partial x} \right| \right\rangle = \frac{n_I}{\mathcal{L}_0}, \tag{4.13}$$

where f_ψ represents the number of turbulent/non-turbulent (non-turbulent/turbulent) transitions n_I per length in the streamwise direction. Following the previous investigations (Debye, Anderson & Brumberger 1957; Thiesset *et al.* 2020; Gauding *et al.* 2021), it can be deduced that $\lim_{r\to 0}(\Theta_I/r) = \langle|\partial\psi/\partial x|\rangle$ from the small-separation limit in (4.12), which means that the small-separation limit of the second-order structure function is equal to the jump frequency. Figure 12(*a*) shows the jump frequency f_ψ as a function of the wall-normal heights for all the cases III-D1–D20. In the plot, f_ψ has a clear maximum for each tripping configuration, which means that the alteration between turbulent and non-turbulent happens most frequently. On increasing the tripping rod diameter, the maximum f_ψ moves outwards with a gradually decreasing trend, meanwhile, the wall-normal span of f_ψ has a broader extent, which implies a growing wall-normal extent of the TNTI in the over-tripped conditions. This is consistent with the results of the intermittency parameters in figure 8. It is shown that, with increasing tripping rod diameter, the intermittency region rapidly extends further away from the wall by holding a wider proportion of the boundary layer (as shown in the inset of figure 12*a*). Specifically, the intermittency parameter exhibits a normal distribution with an increasing standard
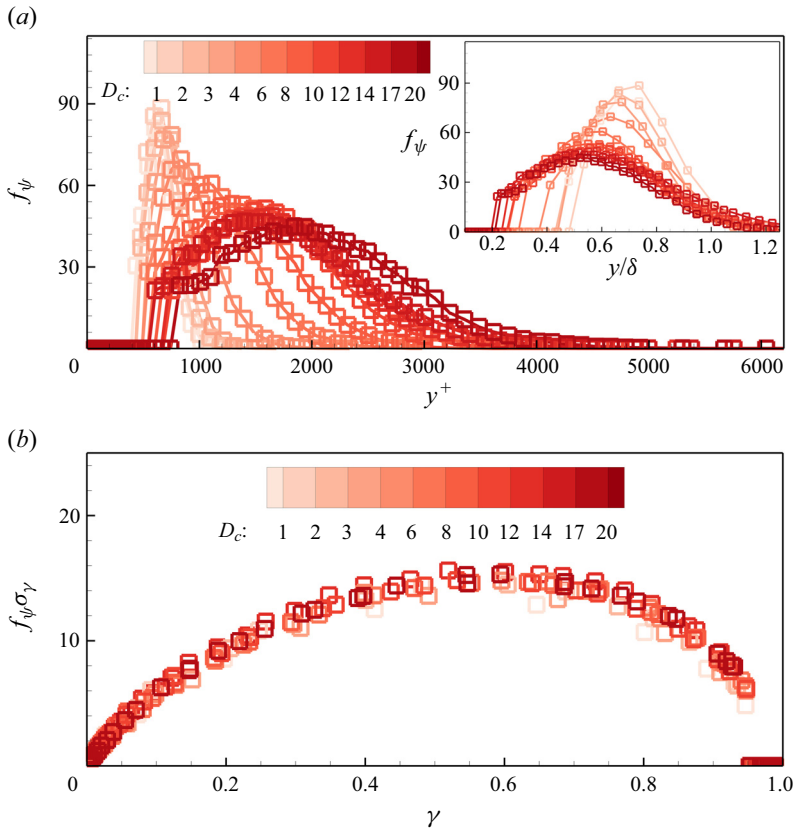
984 A34-18

Figure 12. (*a*) Jump frequency f_ψ as a function of the wall-normal height y^+ (y/δ in the inset), (*b*) self-preservation of f_ψ after normalization with the standard deviation of intermittent parameter σ_γ, as a function of γ. The data are for the various tripping conditions with different rod diameters (cases III-D1–D20). The results of cases I and II are shown in Appendix D.

deviation σ_γ. Here, σ_γ is suggested to be a measure of the width of the intermittent zone. Thus, σ_γ is employed for the normalization in figure 12(*b*), and f_ψ exhibits a self-preserving shape with intermittent factor in the relationship of $f_\psi \sigma_\gamma \propto \gamma$. This finding is consistent with the growth of the characteristic length scale of TNTI with increasing tripping diameter in the framework of self-similar behaviour.

4.3. *Structure functions and the effects of external intermittency*

The current tripping configurations provide a predominant influence on the intermittency in the wake region, such as the jump frequency, which attracts our interest as to whether the self-similarity of the structure functions can be observed in the intermittent zone. Figure 13 shows the normalized even-order structure functions up to the tenth order at the different wall-normal heights for the case III-D20. As shown in figure 13(*a*,*b*), the structure functions are normalized by the Kolmogorov scales (u_K and η) and the Taylor scales (u_λ and λ), respectively, similar to figure 3. It seems that the second order shows the self-similarity as regards the wall-normal heights in the range of $\gamma = 0.1-0.9$, by showing an acceptable collapse in either form of the normalizations. The remarkable collapse is noted at the small scales; the distribution can be explained by the validation
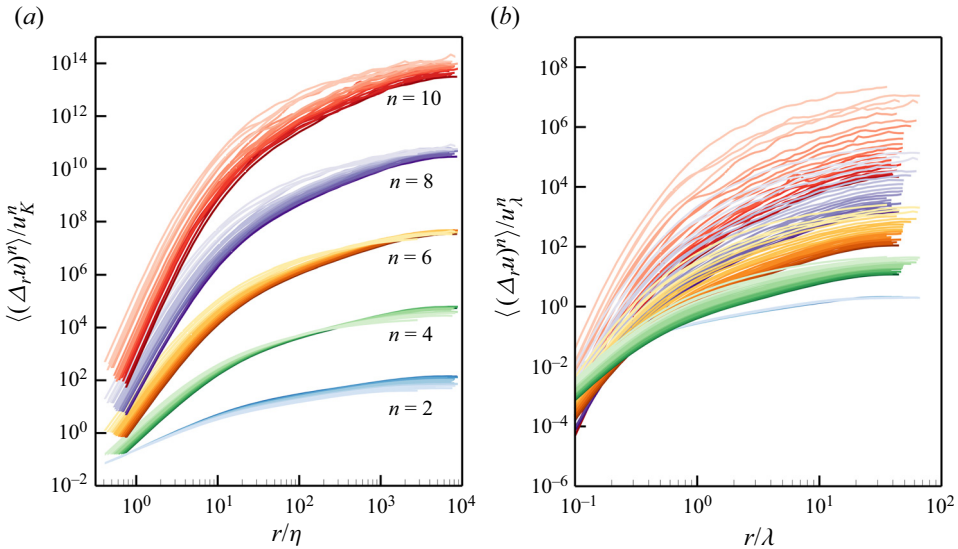
(*a*)

(*b*)

Figure 13. Distribution of even-order structure functions up to the tenth order at different wall-normal heights in the range of $\gamma = 0.1-0.9$ for case III-D20. The structure functions are normalized by (*a*) the Kolmogorov scales and (*b*) the Taylor scales, as similar in figure 3. The line colour from dark to light means that the wall-normal position moves outwards, corresponding to an intermittency parameter from $\gamma = 0.9$ to 0.1.

of classical Kolmogorov scaling. At the large scales, a certain discrepancy is noted in the Kolmogorov-scale normalizations, which should be attributed to the external intermittency in the over-tripped conditions. It is evident that the higher-order structure functions (fourth to tenth order) exhibit a clearly non-collapsing and non-self-similar arrangement over the entire range of scales through the intermittent zone. This result is expected in higher-order statistics, which are very sensitive to various factors, especially external intermittency, and probably promoted under the influence of the tripping conditions. Additionally, by comparing with the results in the inner region, as shown in figure 3(*a*), it is indicated that the spatial resolution effect of the hot-wire probe on the estimation of the Kolmogorov length scale should be neglected from the reasons causing the non-collapsing distribution in figure 13(*a*).

To reveal the cause behind the lack of self-similarity of higher-order structure functions, we present the characteristics of intermittency. Following Batchelor & Townsend (1949), the turbulent signals are intermittent when the fine structure of the turbulence tends to be locally concentrated, intermittent in nature and randomly scattered through the fluid in a spotty way. This spatially spotty pattern becomes more prominent with increasing order of the velocity derivative. Hence, the higher-order moment of velocity derivative is a suitable tool to probe turbulent intermittency, and the flatness is defined as

$$F = \frac{\left\langle \left(\frac{\partial u}{\partial x} \right)^4 \right\rangle}{\left\langle \left(\frac{\partial u}{\partial x} \right)^2 \right\rangle^2}, \tag{4.14}$$

which is widely accepted to represent intermittency at the fine scales. Note that, for the velocity increment $\Delta_r u = u(x + r) - u(x)$, when $r \to 0$, $\Delta_r u$ at small scales is essentially equivalent to the derivative.

For the purpose of testing the original Kolmogorov similarity hypothesis, the evolution of high-order statistics of the velocity derivatives with Re_λ has been widely examined. It was indicated that the statistic of F is affected by two factors, which are the finite-Reynolds-number effect and the flow conditions (Antonia *et al.* 2015, 2017; Djenidi *et al.* 2017; Meldi, Djenidi & Antonia 2018; Tang *et al.* 2018). Figure 14(*a*) shows the distribution of the flatness factor F against Re_λ for all the data with the intermittency parameter in the range of $\gamma = 0.1-0.9$ (for cases III-D1–D20). In the plot, with increasing tripping diameter D_c, both F and Re_λ exhibit a broader extent. Each of the tripping conditions indicates that the flatness factor of the velocity derivative F is increased on reducing Re_λ (also γ). From the numerous investigations, the Re_λ dependence of F in a fitting power law has been sought empirically in different kinds of flows, and the fitting power law $F \sim (1.14 \mp 0.19)Re_\lambda^{0.34 \pm 0.03}$ was derived from an abundance of turbulent data (Antonia, Satyaprakash, & Hussain 1982; Jiménez *et al.* 1993; Wang *et al.* 1996; Sreenivasan & Antonia 1997; Gotoh *et al.* 2002; Ishihara *et al.* 2007; Ishihara, Gotoh & Kaneda 2009). The fitting power law is drawn in figure 14(*a*) for comparison. It can be seen that, at a high intermittent factor ($\gamma \to 0.9$), F shows a good collapse with the power law of Re_λ. The collapse means that the high-order statistics of fine-scale structures in the wall-normal region with the higher γ are almost independent of the impact of external intermittency. The results are supported by Djenidi *et al.* (2017) that a constant flatness factor can be noted in the region $0.3 \leq y/\delta \leq 0.6$ (corresponding to high γ), in which both F and Re_λ are independent of the distance to the wall. On decreasing the intermittent factor (further away from the wall), F has an obvious deviation from the fitting power law of Re_λ by showing significantly greater values in figure 14(*a*), which could be attributed to the effect of the flow conditions of external intermittency. Similarly, figure 14(*b*) shows the dependence of F on the external intermittency parameter γ. As shown, F increases from an inner value close to 6 ($\gamma \to 0.9$) to a value around 50 ($\gamma \to 0.1$) close to the edge of the boundary layer. Considering that the velocity derivative can emphasize the fine-scale components but not cut out the low-frequency (large-scale) parts of the signal (Kuo & Corrsin 1971), the dependence of F confirms that the fine scales do not decouple from the large scales under the tripping effects and further supports that the external intermittency has a dominant impact on the fine scales. In fact, the remarkable change of F was also discussed by Gauding *et al.* (2021) in turbulent jet flows. They linked the change of F to the local kinematics of TNTI by considering the non-equilibrium in the energy cascade and the direction of the inter-scale transport (Watanabe, da Silva & Nagata 2019, 2020), which is probably further promoted in the current over-tripped conditions.

To further understand the impact of external intermittency, the conditional flatness factor of the velocity derivatives is defined as (following the expression of (4.6))

$$F_T = \frac{\left\langle \psi \left(\frac{\partial u}{\partial x} \right)^4 \right\rangle}{\left\langle \psi \left(\frac{\partial u}{\partial x} \right)^2 \right\rangle^2}. \tag{4.15}$$

The binary indicator function of intermittency ψ is introduced to consider only the turbulent portion of the outer-layer flow. Figure 15(*a,b*) shows the distribution of conditional flatness factor F_T against Re_λ and γ, respectively. In figure 15(*a*), F_T and
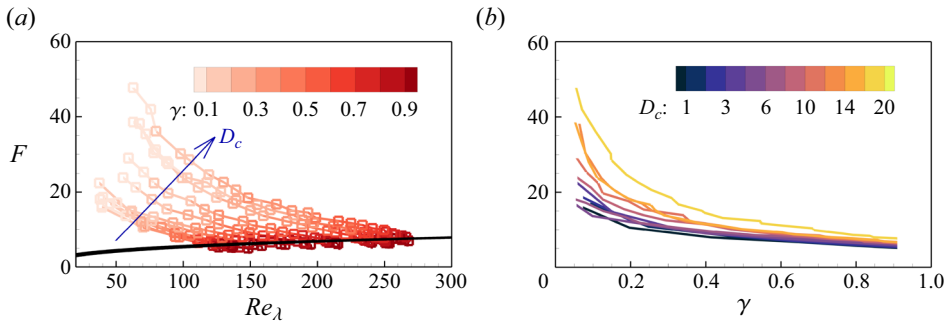
(*a*)

(*b*)

Figure 14. Flatness factor of the velocity gradients F as a function of (*a*) Reynolds number Re_λ (light to dark red colour represents an increase of intermittent parameter from $\gamma = 0.1$ to 0.9, the black line indicates the power law $F = (1.14 \mp 0.19)Re_\lambda^{0.34\pm0.03}$) and (*b*) the intermittency parameter γ (the line colour indicates the tripping rod diameter, D_c).
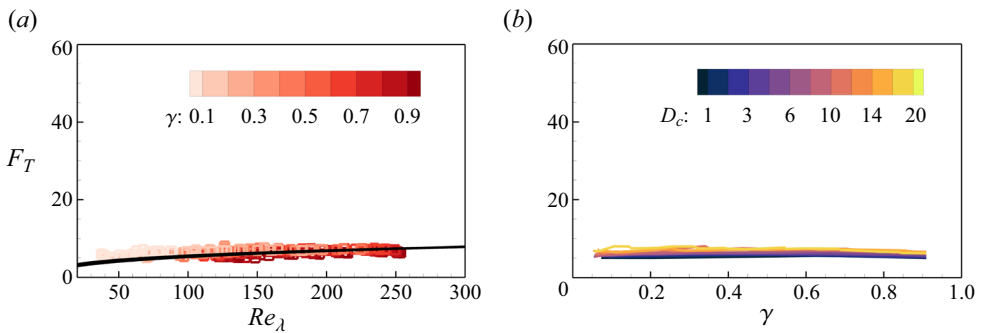
(*a*)

(*b*)

Figure 15. Conditional flatness factor of the velocity gradients F_T as a function of (*a*) Reynolds number Re_λ and (*b*) the intermittency parameter γ. Note that the presentation is completely consistent with that in figure 14 for comparison.

Re_λ show a good agreement with the power law $F_T = (1.14 \mp 0.19)Re_\lambda^{0.34\pm0.03}$ for all the data at different wall-normal heights through the intermittent region. It is clear that the effect of the external intermittency, which leads to the obvious deviation (significantly high values of F in figure 14*a*), is excluded by examining the conditional flatness factor F_T, which is further confirmed by the distribution of the p.d.f.s of the velocity derivatives in figure 16. The power-law dependence of F_T on Re_λ in figure 15(*a*) implies that, in the turbulent regimes of the outer layer, the large-scale fluctuations play a role in determining the turbulence intermittency, the level of which increases with Re_λ (Batchelor & Townsend 1949).

In figure 15(*b*), F_T is almost constant and less sensitive to the variations of γ. Obviously, these findings are independent of the tripping conditions, which means that the strong turbulent transport of the wake flow could lead, in a homogenized statistical sense, to the turbulent regions. The homogenization of turbulent regions was speculated by Corrsin & Kistler (1955) and later confirmed by free shear flows (Mellado *et al.* 2009; Gauding *et al.* 2021). The current results expand this feature into the wall-bounded shear turbulent flows, especially in the over-tripped conditions. In addition, the analogy suggests that the external intermittency has a comparable role in the TNTI in the outer region for both the free and wall-bounded shear flows.
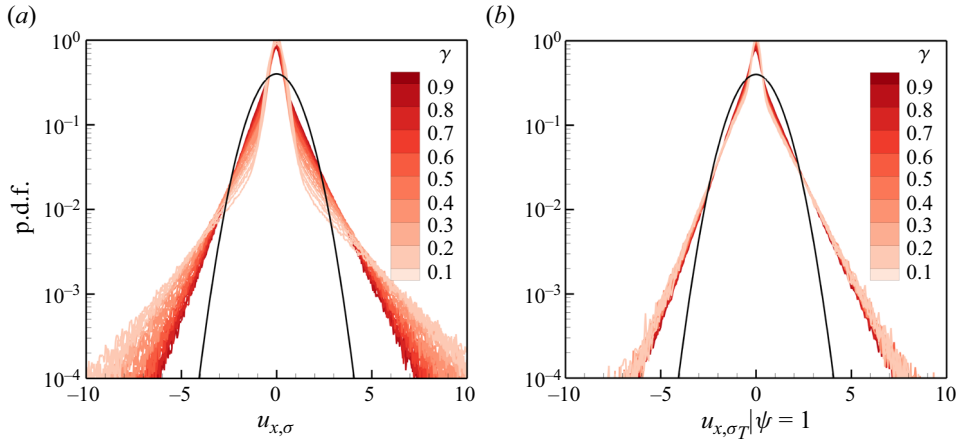
984 A34-22

Figure 16. Conventional (*a*) and conditional (*b*) p.d.f.s of the velocity derivatives at different wall-normal positions as indicated in the legend of intermittent factor γ. The black dashed line indicates a normal distribution. The curves are normalized by the standard deviation $\sigma = \langle(\partial u/\partial x)^2\rangle^{1/2}$ and the conditional standard deviation $\sigma_T = \langle(\psi\,\partial u/\partial x)^2\rangle^{1/2}$, respectively. The density functions are estimated over abscissa intervals of bin width 0.15σ ($0.15\sigma_T$). Data for case III-D20.

To reveal the mechanism behind the fine-scale coupling related to the external intermittency, we study the p.d.f.s of the velocity derivatives at different wall-normal heights through the intermittent zone. In fact, the flatness factor of the velocity derivatives can be obtained in the integral expression as

$$F = \int_{-\infty}^{\infty} (u_{x,\sigma})^4 \sigma P(u_{x,\sigma})\,\mathrm{d}u_{x,\sigma}, \tag{4.16}$$

where $u_{x,\sigma} = (\partial u/\partial x)/\sigma$, $P(u_{x,\sigma})$ is the p.d.f. of the normalized velocity derivative and $\sigma = \langle(\partial u/\partial x)^2\rangle^{1/2}$ is the standard deviation. Figure 16(*a*) shows the p.d.f.s of the velocity derivative $(\partial u/\partial x)/\sigma$ at the different wall-normal heights through the intermittent zone. Since the fourth moment is heavily dependent on the large values of $u_{x,\sigma}$, the flatness factor F in figure 14 is a measure of the relative extent of the skirts of the probability density curves. Clearly, it can be seen in figure 16(*a*) that the p.d.f.s depart from normality further away from the wall towards the boundary-layer edge. The departure is enhanced by showing that the tails of $P(u_{x,\sigma})$ become increasingly stretched, which is a characteristic footprint of the external intermittency. In particular, the far tails represent large velocity gradients that partly stem from the thin interfacial layer between turbulent and non-turbulent fluids (Elsinga & da Silva 2019). At the same time, a distinct peak emerges around $u_{x,\sigma} = 0$. This peak originates from non-turbulent regions outside of the turbulent envelope where the velocity gradients are close to zero. The combination of these behaviours leads to the flatness factor F increasing as it moves toward the boundary-layer edge, as shown in figure 14.

It is now of interest to compare the results with the conditional p.d.f.s that account only for the turbulent portion of the flow. The conditional p.d.f. is defined as $P(u_{x,\sigma_T}|\psi = 1)$ in the condition of $\psi = 1$. A similar procedure was executed by Gauding *et al.* (2021) to observe the self-similarity in the shear-layer region of turbulent jet flows. The parameter $P(u_{x,\sigma_T}|\psi = 1)$ in figure 16(*b*) exhibits self-similarity. The departure from normality has the same shape, which has a higher probability than the normal curve in the neighbourhood of zero and a lower probability at the intermediate values. This kind of distribution
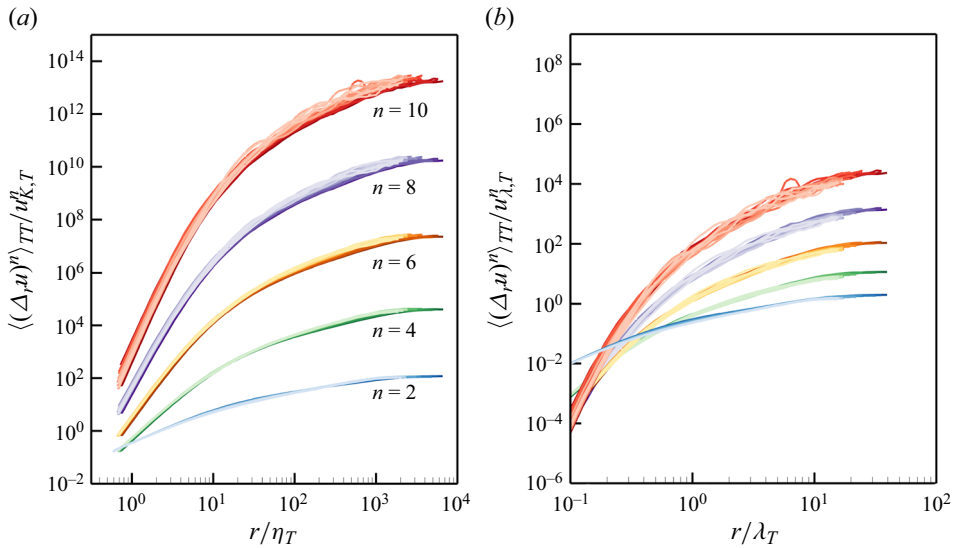
Figure 17. Normalized conditional structure functions $\langle(\Delta_r u)^n\rangle_{TT}$ up to the tenth order at different wall-normal heights, where both end points are located inside the turbulent regime. The structure functions are normalized by the conditional (*a*) Kolmogorov scales and (*b*) Taylor scales. The line colour has the same meaning as that in figure 13. Data for case III-D20.

was consolidated as a typical feature of turbulent signals with internal intermittency in the inner region of TBL flow (Kuo & Corrsin 1971), similar to figure 4. From this comparison between figure 16(*a,b*), we can conclude that external intermittency is the relevant mechanism that destroys self-similarity through the intermittent zone.

Finally, we revisit the self-similarity of the velocity structure functions. Motivated by the previous discussion, a conditional structure function is defined as

$$\langle(\Delta_r u)^n\rangle_{TT} = \langle\psi(x+r)\psi(x)(u(x+r)-u(x))^n\rangle, \tag{4.17}$$

for which both ending points are restricted to the turbulent regime of the boundary layer. In the previous investigation, Sabelnikov *et al.* (2019) defined structure functions in a similar fashion to distinguish in non-premixed flames between burnt and unburnt regions.

Figure 17 presents the normalized conditional structure functions $\langle(\Delta_r u)^n\rangle_{TT}$ up to the tenth order at different wall-normal heights through the intermittent zone. The structure functions are normalized by conditional Kolmogorov scales ($u_{K,T} = (\nu\langle\psi\epsilon\rangle)^{1/4}$ and $\eta_T = (\nu^3/\langle\psi\epsilon\rangle)^{1/4}$) and conditional Taylor scales ($u_{\lambda,T} = \langle\psi u^2\rangle^{1/2}$ and $\lambda_T = (15\nu u_{\lambda,T}^2/\langle\psi\varepsilon\rangle)^{1/2}$) that account only for the turbulent portion of the flow. Compared with the conventional structure functions $\langle(\Delta_r u)^n\rangle$ (in figure 13), the conditional structure functions $\langle(\Delta_r u)^n\rangle_{TT}$ reveal a significantly improved collapse up to the tenth order, as shown in figure 17(*a,b*). Especially, on increasing the order, the self-similar arrangement can still be noted. In this sense, $\langle(\Delta_r u)^n\rangle_{TT}$ is assumed to have a reasonably good universality. More importantly, the observation signifies that turbulent regions homogenize across the intermittent zone even under the most over-tripped condition.

Considering the collapse of the conditional high-order structure functions, we now examine the scaling exponents of structure functions and external intermittency in the following. Other than the turbulent signal in the near-wall region, the turbulent signals in the intermittent zone are dominated by external intermittency, the behaviour of which is
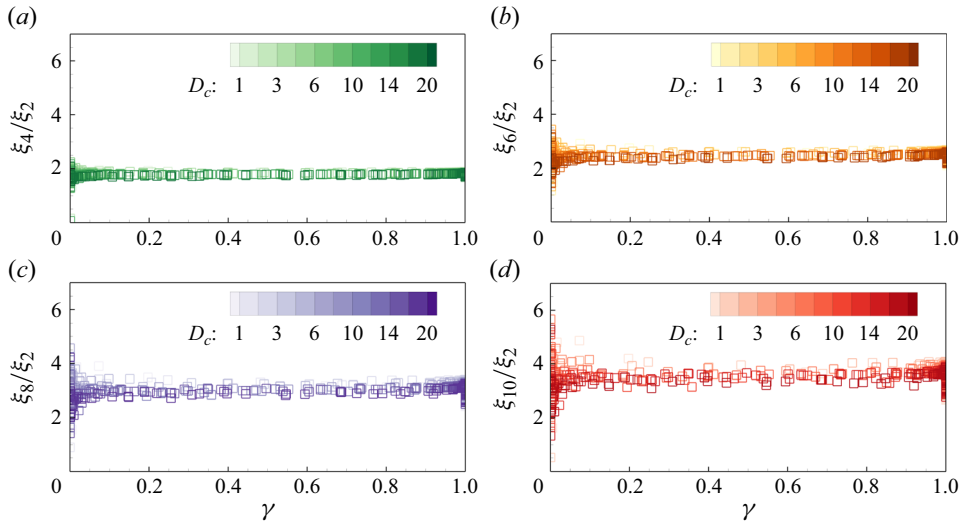
Figure 18. Dependence of the relative scaling exponents ξ_p/ξ_2 on the intermittency parameter γ for all the tripping conditions (cases III-D1–D20) and for (*a*) $p = 4$, (*b*) $p = 6$, (*c*) $p = 8$, (*d*) $p = 10$.

enhanced by the tripping configurations. Thus, the self-preservation/similarity behaviour of the conditional higher-order structure functions will not be examined for the ECR scales but rather examined in a relative scaling form by the ESS hypothesis as

$$
\frac{\xi_p}{\xi_2} = \frac{\mathrm{d}\log\langle(\Delta_r u_T)^p\rangle}{\mathrm{d}\log\langle(\Delta_r u_T)^2\rangle}, \tag{4.18}
$$

which is calculated by the gradient of the *p*th-order conditional structure function against the second order. The ESS approach in (4.18) provides an extended wide scaling range relative to the restricted subrange, which offers an opportunity for better estimates of the relative ISR scaling exponents (Benzi *et al.* 1993*a,b*). Figure 18 shows the scaling exponents ξ_p/ξ_2 ($p = 4$, 6, 8, 10) at different wall-normal heights. It shows ξ_p/ξ_2 as a function of the external intermittency parameter γ. Clearly, the relative scaling exponents remain constant with γ and collapse for all the tripping cases. This result indicates that the small scales in turbulent regimes are homogenized in a self-similar behaviour, which is independent of the wall-normal height and the influence of the current tripping wake flows.

Furthermore, the *p*-model, $\xi_p = 1 - \log_2(0.7^{p/3} + 0.3^{p/3})$, developed by Meneveau & Sreenivasan (1991), is employed for comparison. The *p*-model is based on a multi-fractal approach and is known to be able to predict the ISR scaling exponents of homogeneous isotropic turbulence with very good accuracy (Sreenivasan & Antonia 1997). Figure 19 plots the average relative scaling exponents (as shown in figure 18) through the intermittent zone $\gamma = 0.1-0.9$ for cases I, II and III. The plot shows an acceptable agreement with the prediction from the *p*-model. Hence, the relative scaling exponents confirm the self-similarity of higher-order structure functions in the turbulent regime even under the influence of the over-tripped conditions. In addition, the average relative scaling exponents in figure 19 involve the cases at all Reynolds numbers in this study, the agreement indicates that the self-similarity of higher-order structure functions is independent of the current Reynolds numbers.
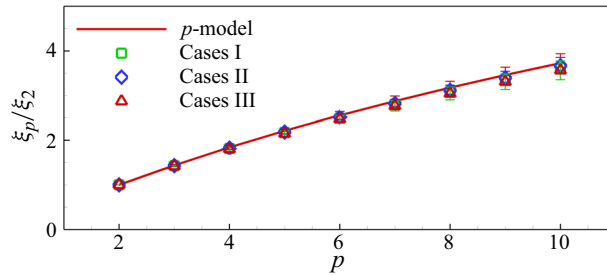
Figure 19. The average of relative scaling exponents ξ_p/ξ_2 up to the tenth order in the intermittent zone $\gamma = 0.1-0.9$ for cases I, II and III. The standard deviation is denoted by the error bar. For comparison, the p-model, $\xi_p = 1 - \log_2(0.7^{p/3} + 0.3^{p/3})$, by Meneveau & Sreenivasan (1991) (solid line) is shown.

5. Conclusions

In artificially thickened TBL flows from over-tripped conditions, the generated large-scale structures not only alter the intermittency behaviour in the outer region but also provide a modification to the small scales in the inner region. Thus, the effect of the internal and external intermittencies on the self-similarity of TBL in the adaptive region was examined in this study.

In the inner region, by utilizing the ESS hypothesis, the relative scaling of the velocity structure functions was presented with a further reaching universality for the ECR scales. The scaling for the ratio between the velocity structure functions was based on the log-law scaling for the ECR scales in the logarithmic region of high-Reynolds-number TBLs (Davidson *et al.* 2006; de Silva *et al.* 2015, 2017), which is in accordance with Townsend's attached eddy hypothesis. The current study consolidated that the quantitative measures of the scaling behaviour for the ECR scales can be effectively estimated from databases at low and moderate Reynolds numbers ($Re_\tau \approx 500-3500$). Moreover, in the current over-tripped conditions, the boundary layer is thickened with increasing tripping rod diameter, and the constant exponent scaling extends further away from the wall. It can be concluded that the scaling universality for the ECR scales in ESS form is independent of the tripping conditions, which is enhanced with a further reaching universality in the over-tripped conditions.

Then, we studied the self-similarity of structure functions at different wall-normal positions through the intermittent zone. In the intermittent zone, the phenomenon of external intermittency originates from the TNTI, which separates the turbulent and non-turbulent regimes from the hot-wire signals. The morphology of the TNTI was described by the intermittency structure function at different scales. It was indicated that the over-tripped conditions provide a significant modification to the external intermittency. Even though the non-Gaussianity and external intermittency are enhanced under the over-tripped impacts, an acceptable self-similarity was noted for the second-order velocity structure functions through the outer region. However, it was expected that the external intermittency exhibits a remarkable influence on the high-order structure functions. The breakdown of self-similarity was mainly contributed to by the combination of the appearance of higher velocity derivatives and the alternation of turbulent and non-turbulent fluids, which was supported by corresponding statistics such as the flatness factor of velocity derivatives and the jump frequency of turbulence–non-turbulence (*vice versa*). In fact, the effect of external intermittency on fine-scale turbulence was amplified by increasing the tripping rod diameter. It was manifested that the fine scales are not

decoupled with the large scales which are related to the external intermittency at all the tripping conditions.

By defining the turbulent statistics conditioned on fully turbulent regimes, the collapse was noted in the conditional flatness factor and the p.d.f.s of the velocity derivatives, which are nearly independent of the intermittency parameter γ. Then, the self-similarity behaviour of the conditional higher-order structure functions was further examined. The relative scaling exponents obtained by the ESS hypothesis remain constant against the intermittency parameter across the intermittent zone. An agreement of the conditional scaling exponents with the *p*-model was further examined. It was revealed that the fine scales in the turbulent regime in the artificially thickened TBLs are homogenized in a self-similar behaviour, which is independent of the tripping conditions and also the Reynolds number in the current study. In addition, it should be noted that the above conclusions of the scaling universality of the structure functions are also suitable for the canonical cases, as moderately tripped TBLs with relatively small tripping diameters were involved in the current study.

In practice, the TBL flows over wind turbines, ships, vehicles and aviation systems, experience the effects of leading-edge configurations or upstream flow conditions (such as, roughness, surface curvature, separation, blowing, suction, etc.). Thus, the practical TBL flows are not only at the condition of high Reynolds number, but also beyond canonical flows with the feature of significant changes in all aspects of the mean flow and the turbulence. The current study presents evidence of the self-similarity of non-canonical TBL flows at relatively high Re_τ under leading-edge tripping impacts. With regards to this, the observation in this study provides a potential avenue to assess/predict more general and practical TBL flow behaviour.

Author ORCIDs.
 Zhanqi Tang https://orcid.org/0000-0002-5631-2949.

Appendix A. Amplitude and frequency modulation

To explore the amplitude and frequency modulation (AM and FM) effect of the large-scale structure on the small scales in TBL flows, various methods have been used in the previous works (Mathis *et al.* 2009; Ganapathisubramani *et al.* 2012; Baars *et al.* 2015; Dogan *et al.* 2019; Iacobello, Ridolfi & Scarsoglio 2021). The main objective is to identify a characteristic measure to quantify the instantaneous amplitude/frequency of the small scales. Baars *et al.* (2015) applied continuous wavelet transform (CWT) to obtain the wavelet power spectrum of the fluctuations in time–frequency space, and then constituted a series of instantaneous amplitude and frequency signals for the observation of AM and FM effects. In this study, we also utilize the CWT method to observe the AM and FM effects under the tripping impact.

To obtain the large and small scales, based on a filter cutoff of $\lambda_x^+ = 2000$, the fluctuations are decomposed into large scales, u_L ($\lambda_x^+ > 2000$) and small scales, u_S ($\lambda_x^+ < 2000$). This cutoff length is inferred from the discrepancy of the energy spectra, as shown in figure 21, which clearly segments the large-scale structures in the

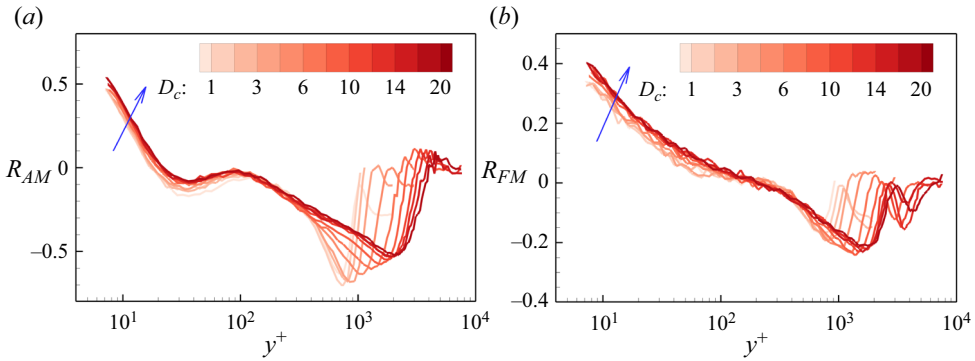Figure 20. The distributions of (*a*) amplitude modulation and (*b*) frequency modulation coefficients between the large and small scales along the wall-normal locations for the tripping cases III-D1–D20.

over-tripped conditions. Then, by convolving with a mother wavelet (ψ), the fluctuation signals (u) are decomposed into a time–frequency space as $\tilde{u}(t', s) = (1/\sqrt{s}) \int_{-\infty}^{\infty} u(t) \psi((t - t')/s) \, dt$, where s indicates wavelet time scales. In this study, the Morlet wavelet is employed as the mother wavelet. It has been confirmed that the modulation results are robust to the different mother wavelets, such as Morlet and Mexican hat wavelets (Baars *et al.* 2015). Then, the wavelet power spectrum (WPS) is calculated as, $\tilde{E}(t', s) = |\tilde{u}(t', s)|^2/s$. By transforming wavelet time scale to an equivalent frequency, the WPS is given by $\tilde{E}(t', f)$. The small-scale amplitude time series can be constructed by integrating the WPS as $\sigma_S(t') = \left(\int_{f_S}^{f_N} \tilde{E}(t', f) \, df \right)^{1/2}$, where f_S and f_N represent the small-scale cutoff frequency and Nyquist frequency, respectively. The fluctuation form of $\sigma_S(t')$ is calculated by $\sigma_S'(t') = \sigma_S(t') - u_S^2$. Then, the large-scale variation of small-scale amplitude $\sigma_{S,L}'(t')$ is obtained with the long wavelength pass filter of $\lambda_x^+ > 2000$, which is the representative of the instantaneous small-scale amplitude. On the other hand, the small-scale instantaneous frequency $f_S(t')$ is calculated as $f_S(t') = 10^{F(t')}$, in which $F(t') = \int_{f_S}^{f_N} \tilde{E}(t', f) f \log_{10}(f) \, d \log_{10}(f)/(\sigma_S(t'))^2$. The fluctuation signals of $f_S(t')$ is decomposed as $f_S'(t') = f_S(t') - \langle f_S \rangle$, where $\langle f_S \rangle$ is the mean of $f_S(t')$. Then, the pass filter of $\lambda_x^+ > 2000$ is applied again for evaluating the large-scale variation of small-scale frequency ($f_{S,L}'(t')$). After that, the cross-correlation algorithm is employed to observe the AM and FM effects, as $R_{AM} = \langle u_L \sigma_{S,L}' \rangle / \sqrt{\langle u_L^2 \rangle \langle \sigma_{S,L}'^2 \rangle}$ and $R_{FM} = \langle u_L f_{S,L}' \rangle / \sqrt{\langle u_L^2 \rangle \langle f_{S,L}'^2 \rangle}$, respectively.

Figure 20(*a,b*) shows the distributions of the amplitude and frequency modulation coefficients along the wall-normal locations for all the tripping cases III-D1–D20. In figure 20(*a*), the AM coefficients present the positive value in the near-wall region, which means that the higher small-scale amplitude occurs in high-speed large-scale motions, and *vice versa* (Mathis *et al.* 2013; Hutchins 2014; Baars *et al.* 2017; Dogan *et al.* 2019; Li *et al.* 2023). Under the tripping effect, the growth of near-wall R_{AM} with increasing D_c reveals that the generated large scales have an enhanced AM effect on the small scales. The enhanced FM effects due to the tripping effect can also be noted by showing the increased R_{FM} in figure 20(*b*). This implies that the generated large-scale structures enhance the near-wall FM process by the splatting mechanism (Agostini & Leschziner 2019), similar to the consequence of increasing Re_τ in canonical TBL flows (Baars *et al.* 2015; Iacobello *et al.* 2021). On the contrary, negative R_{AM} and R_{FM} are observed in the outer region, which is interpreted as a reversed scale arrangement phenomenon related
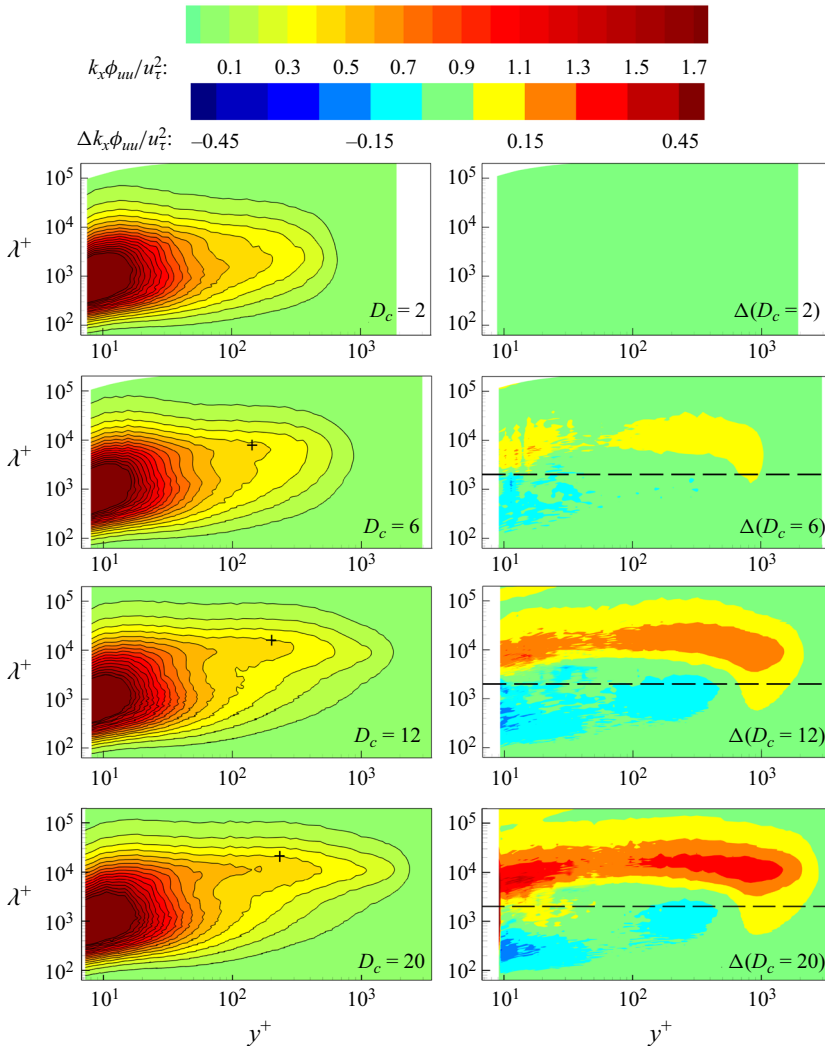
984 A34-28

Figure 21. Pre-multiplied velocity spectra of the fluctuation signal for various tripping diameters for the representative cases III-D2, D6, D12 and D20; in the corresponding right-hand panels, the changes in spectrograms relative to case III-D2 are shown, which are labelled as $\Delta(D_c = 2, 6, 12, 20)$ in each panel. The horizontal dashed line represents the wavelength of $\lambda_x^+ = 2000$. The '+' symbol refers to the proposed outer peak of $y^+ \approx 3.9Re_\tau^{1/2}$ and $\lambda_x/\delta_{D_{c2}} \approx 6$ (Mathis *et al.* 2009).

to the outer-layer intermittency (Baars *et al.* 2017; Tang *et al.* 2021). They are modified under the tripping impacts, meaning that the intermittency is altered due to the generated large-scale structures. In addition, a 'phase reversal' as expected appears in the log layer between the near-wall region and intermittent region (Chung & McKeon 2010).

Appendix B. Evidence of footprint of large scales in the near-wall region

Figure 21 shows pre-multiplied spectra of streamwise fluctuations $k_x\phi_{uu}/u_\tau^2$ as contour plots for several representative cases III-D2, D6, D12 and D20. It can be seen that, on increasing D_c, the pre-multiplied spectra in the outer region present the enhanced
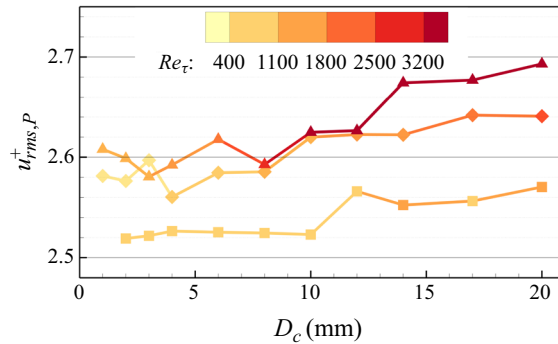
Figure 22. The distribution of the near-wall peak $u^+_{rms,P}$ of the turbulent intensity as a function of tripping diameters D_c for all the cases. The symbols of square, diamond and delta represent cases I, II and III respectively. The symbol colour indicates the corresponding Re_τ.

magnitude with the longer wavelength. Hutchins & Marusic (2007b) proposed that the scale separation starts to appear for $Re_\tau \gtrsim 2000$, with the emergence of the outer energy site. This estimate is consistent with the current cases of $D_c = 12-20$ mm ($Re_\tau = 2670-3580$) by showing the outer energy site. It is deduced that the trip wire introduces large-scale energetic motions into the boundary layer. These generated large scales have a comparable length scale to the very-large-scale structures in canonical high-Re_τ TBL flows, which have an outer peak in the spectrogram that emerges at $y^+ \approx 3.9Re_\tau^{1/2}$ and $\lambda_x/\delta \approx 6$ (Hutchins & Marusic 2007a; Mathis *et al.* 2009). Note that this location is marked by '+' in figure 21, which is used purely as a reference to compare with the current over-stimulated cases. Then, the case III-D2 is chosen as the reference case by considering its nominal canonical behaviour, to observe the differences in the pre-multiplied spectra, as $\Delta k_x \phi_{uu}/u_\tau^2 = k_x \phi_{uu}/u_{\tau D_c=N}^2 - k_x \phi_{uu}/u_{\tau D_c=2}^2$, where $N = 6$, 12, 20. The composite spectrum of case III-D2 is re-gridded by cubic interpolation to the range of the spectrum in the other cases prior to the subtraction. As expected, the increasing excess energy with D_c is observed in the outer region. Look carefully, the outer-layer excess energy is pre-dominantly located near $\lambda_x^+ \approx 6 \times 10^3 - 2 \times 10^4$ ($\lambda_x/\delta_2 \approx 7-23$). This suggests that the over-tripped conditions introduce large-scale motions which almost take over the outer layer. Moreover, the enhanced large-scale energy in the near-wall region seems to be the derivative of these energetic outer-layer large scales, and the extent of the penetration depends on the tripping intensity. This refers to the generated large scales penetrating down to the wall based on the footprint effect (Hutchins & Marusic 2007b; Baars *et al.* 2017), which leads to the increasing near-wall peak in the broadband turbulence intensity, as shown in figure 22. Figure 22 shows the distribution of the near-wall peak of the turbulence intensity, $u^+_{rms,P}$, as a function of tripping diameter D_c for the cases I, II and III. Caution must be exercised when examining the near-wall peak due to the spatial and temporal resolution challenges of the hot-wire probe (Ligrani & Bradshaw 1987; Hutchins *et al.* 2009). Based on the current hot-wire spatial resolution, it can be still observed that, for each free-stream velocity, increasing D_c results in the growth of $u^+_{rms,P}$, which is attributed to a growing superposition of the generated larger-scale energy in the near-wall region. In addition, the growth of $u^+_{rms,P}$ can be also noted with increasing Re_τ, as widely reported in canonical TBL flows (Metzger & Klewicki 2001; Hoyas & Jiménez 2006; Hutchins *et al.* 2009).
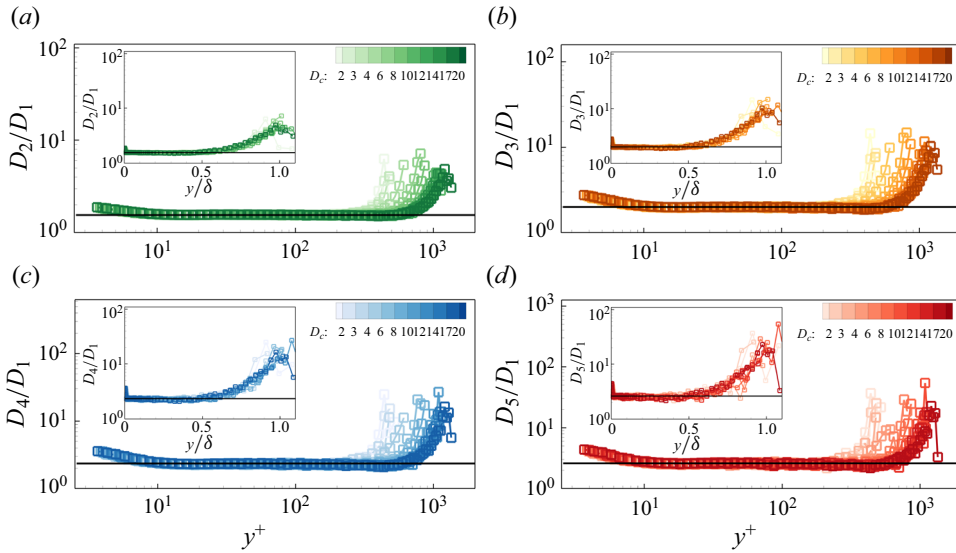
Figure 23. Distribution of ratios D_p/D_1 along y^+ (y/δ in the insets) for cases I-D2–D20; (*a*) $p = 2$, (*b*) $p = 3$, (*c*) $p = 4$ and (*d*) $p = 5$. For comparison, the black lines represent the coefficient ratio value calculated from the DNS TBL datasets from Sillero *et al.* (2013) ($z^+ \approx 150$, $Re_\tau \approx 1600$).
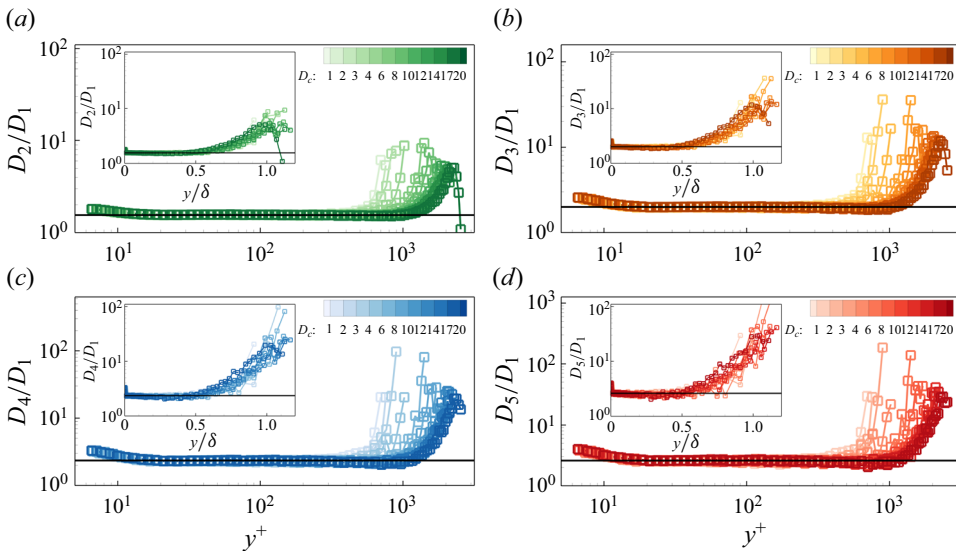

Figure 24. Distribution of D_p/D_1 along y^+ (y/δ in the insets) for cases II-D1–D20; (*a*) $p = 2$, (*b*) $p = 3$, (*c*) $p = 4$ and (*d*) $p = 5$. Consistent presentation as in figures 7 and 23.

Appendix C. Scaling universality of ECR scales

The distribution of ratios D_p/D_1 ($p = 2,\ 3,\ 4,\ 5$) across the entire boundary layer for the tripping cases I-D2–D20 and II-D1–D20, are shown in figures 23 and 24. By comparing the results in cases I, II and III, we confirm that the scaling universality of the ECR scales is independent of the incoming Reynolds numbers in the current study. Moreover, consistent conclusions can be derived from the plots that the scaling universality of ECR scales is
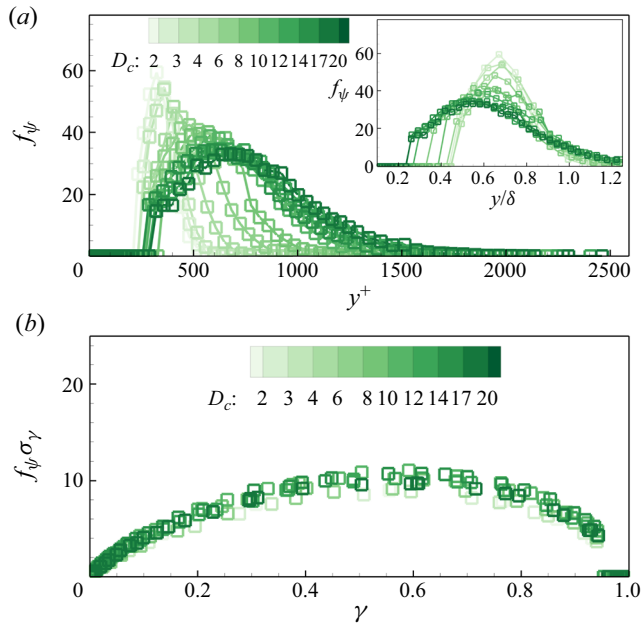
Figure 25. (*a*) Jump frequency f_ψ as a function of y^+ (y/δ in the insets), (*b*) normalized jump frequency $f_\psi \sigma_\gamma$ as a function of γ. Data for cases I-D2–D20.
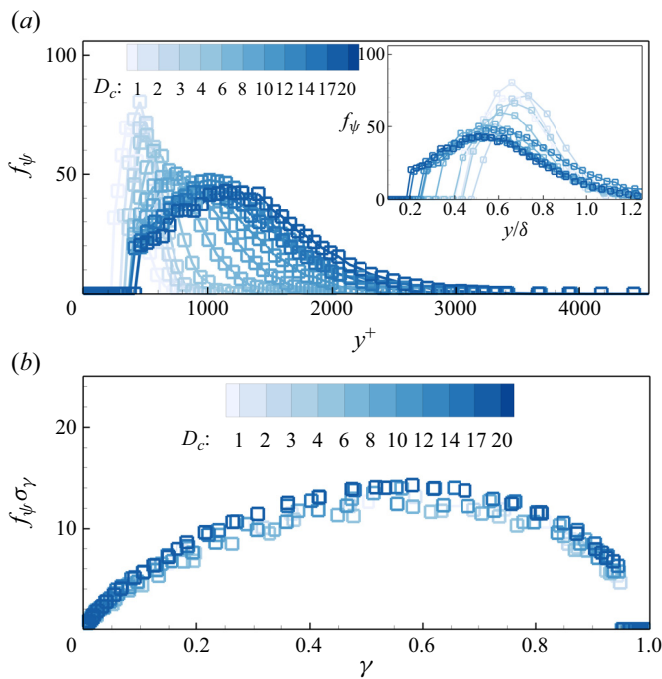

Figure 26. Consistent results of the data for cases II-D1–D20, as in figures 12 and 25.

independent of the tripping rod diameter, and a further reaching of universality with a larger wall-normal extent can be noted on increasing the rod diameter. On the other hand, the obvious discrepancy can be noted in the outer region around the edge of the boundary layer, which is dominated by the intermittency of generated large-scale structures from the tripping configurations.

Appendix D. Jump frequency

Figure 25 shows the jump frequency as a function of y^+ (y/δ in the insets) and γ for the cases I-D2–D20. The corresponding results for cases II-D1–D20 are shown in figure 26. The consistent indications can be obtained from figures 25, 26 and 12. The wall-normal span of f_ψ has a broader extent on increasing the tripping intensity. Moreover, an acceptable agreement of the relation $f_\psi \sigma_\gamma \propto \gamma$ can be observed for all the tripping conditions, which suggests a self-preserving shape of the TNTI interface under the over-tripped impacts.

REFERENCES

AGOSTINI, L. & LESCHZINER, M. 2019 On the departure of near-wall turbulence from the quasi-steady state. *J. Fluid Mech.* **871**, R1.

ANSELMET, F., GAGNE, Y., HOPFINGER, E.J. & ANTONIA, R.A. 1984 High-order velocity structure functions in turbulent shear flows. *J. Fluid Mech.* **140**, 63–89.

ANTONIA, R.A., DJENIDI, L., DANAILA, L. & TANG, S.L. 2017 Small scale turbulence and the finite Reynolds number effect. *Phys. Fluids* **29**, 020715.

ANTONIA, R.A., SATYAPRAKASH, B.R. & HUSSAIN, A.K.M.F. 1982 Statistics of fine-scale velocity in turbulent plane and circular jets. *J. Fluid Mech.* **119**, 55–89.

ANTONIA, R.A., TANG, S.L., DJENIDI, L. & DANAILA, L. 2015 Boundedness of the velocity derivative skewness in various turbulent flows. *J. Fluid Mech.* **781**, 727–744.

BAARS, W.J., HUTCHINS, N. & MARUSIC, I. 2017 Reynolds number trend of hierarchies and scale interactions in turbulent boundary layers. *Phil. Trans.* A*, Mathe. Phys. Engng Sci.* **375**, 20160077.

BAARS, W.J., TALLURU, K.M., HUTCHINS, N. & MARUSIC, I. 2015 Wavelet analysis of wall turbulence to study large-scale modulation of small scales. *Exp. Fluids* **56**, 188.

BATCHELOR, G.K. & TOWNSEND, A.A. 1949 The nature of turbulent motion at large wave-numbers. *Proc. R. Soc. Lond.* A*, Math. Phys. Sci.* **199**, 238–255.

BENZI, R., CILIBERTO, S., BAUDET, C., CHAVARRIA, G.R. & TRIPICCIONE, R. 1993*a* Extended self-similarity in the dissipation range of fully developed turbulence. *Europhys. Lett.* **24**, 275–279.

BENZI, R., CILIBERTO, S., TRIPICCIONE, R., BAUDET, C., MASSAIOLI, F. & SUCCI, S. 1993*b* Extended self-similarity in turbulent flows. *Phys. Rev.* E **48**, R29–R32.

BISSET, D.K., HUNT, J.C.R. & ROGERS, M.M. 2002 The turbulent/non-turbulent interface bounding a far wake. *J. Fluid Mech.* **451**, 383–410.

BUXTON, O.R.H., EWENZ ROCHER, M. & RODRÍGUEZ-LÓPEZ, E. 2018 Influence of strong perturbations on wall-bounded flows. *Phys. Rev. Fluids* **3**, 014605.

CASTILLO, L. & JOHANSSON, T.G. 2002 The effects of the upstream conditions on a low Reynolds number turbulent boundary layer with zero pressure gradient. *J. Turbul.* **3**, N31.

CHAUHAN, K., PHILIP, J., DE SILVA, C.M., HUTCHINS, N. & MARUSIC, I. 2014 The turbulent/non-turbulent interface and entrainment in a boundary layer. *J. Fluid Mech.* **742**, 1–33.

CHAUHAN, K.A., MONKEWITZ, P.A. & NAGIB, H.M. 2009 Criteria for assessing experiments in zero pressure gradient boundary layers. *Fluid Dyn. Res.* **41**, 021404.

CHEN, C.-H.P. & BLACKWELDER, R.F. 1978 Large-scale motion in a turbulent boundary layer: a study using temperature contamination. *J. Fluid Mech.* **89**, 1–31.

CHEN, L., FAN, Z., TANG, Z., WANG, X., SHI, D. & JIANG, N. 2023 Outer-layer coherent structures from the turbulent/non-turbulent interface perspective at moderate Reynolds number. *Exp. Therm. Fluid Sci.* **140**, 110760.

CHUNG, D. & MCKEON, B.J. 2010 Large-eddy simulation of large-scale structures in long channel flow. *J. Fluid Mech.* **661**, 341–364.

CORRSIN, S. & KISTLER, A.L. 1955 Free-stream boundaries of turbulent flows. NASA-TR-1244.

DAVIDSON, P.A., NICKELS, T.B. & KROGSTAD, P.Å. 2006 The logarithmic structure function law in wall-layer turbulence. *J. Fluid Mech.* **550**, 51–60.

DEBYE, P., ANDERSON, H.R. & BRUMBERGER, H. 1957 Scattering by an inhomogeneous solid. II. The correlation function and its application. *J. Appl. Phys.* **28**, 679–683.

DJENIDI, L., ANTONIA, R.A., TALLURU, M.K. & ABE, H. 2017 Skewness and flatness factors of the longitudinal velocity derivative in wall-bounded flows. *Phys. Rev. Fluids* **2**, 064608.

DOGAN, E., HANSON, R.E. & GANAPATHISUBRAMANI, B. 2016 Interactions of large-scale free-stream turbulence with turbulent boundary layers. *J. Fluid Mech.* **802**, 79–107.

DOGAN, E., ÖRLÜ, R., GATTI, D., VINUESA, R. & SCHLATTER, P. 2019 Quantification of amplitude modulation in wall-bounded turbulence. *Fluid Dyn. Res.* **51**, 011408.

ELSINGA, G.E. & DA SILVA, C.B. 2019 How the turbulent/non-turbulent interface is different from internal turbulence. *J. Fluid Mech.* **866**, 216–238.

ERM, L.P. & JOUBERT, P.N. 1991 Low-Reynolds-number turbulent boundary layers. *J. Fluid Mech.* **230**, 1–44.

FAN, D., XU, J., YAO, M.X. & HICKEY, J.-P. 2019 On the detection of internal interfacial layers in turbulent flows. *J. Fluid Mech.* **872**, 198–217.

FERNHOLZ, H.H. & FINLEYT, P.J. 1996 The incompressible zero-pressure-gradient turbulent boundary layer: an assessment of the data. *Prog. Aerosp. Sci.* **32**, 245–311.

FIEDLER, H. & HEAD, M.R. 1966 Intermittency measurements in the turbulent boundary layer. *J. Fluid Mech.* **25**, 719–735.

FITZHUGH, R. 1983 Statistical properties of the asymmetric random telegraph signal, with applications to single-channel analysis. *Math. Biosci.* **64**, 75–89.

FRISCH, U. 1995 *Turbulence, the Legacy of A.N. Kolmogorov*. Cambridge University Press.

GANAPATHISUBRAMANI, B., HUTCHINS, N., MONTY, J.P., CHUNG, D. & MARUSIC, I. 2012 Amplitude and frequency modulation in wall turbulence. *J. Fluid Mech.* **712**, 61–91.

GAUDING, M., BODE, M., BRAHAMI, Y., VAREA, É. & DANAILA, L. 2021 Self-similarity of turbulent jet flows with internal and external intermittency. *J. Fluid Mech.* **919**, A41.

GOTOH, T., FUKAYAMA, D. & NAKANO, T. 2002 Velocity field statistics in homogeneous steady turbulence obtained using a high-resolution direct numerical simulation. *Phys. Fluids* **14**, 1065–1081.

GROSSMANN, S., LOHSE, D. & REEH, A. 1997 Application of extended self-similarity in turbulence. *Phys. Rev.* E **56**, 5473–5478.

GUALA, M., HOMMEMA, S.E. & ADRIAN, R.J. 2006 Large-scale and very-large-scale motions in turbulent pipe flow. *J. Fluid Mech.* **554**, 521.

HEDLEYT, T.B. & KEFFER, J.F. 1974 Some turbulent/non-turbulent properties of the outer intermittent region of a boundary layer. *J. Fluid Mech.* **64**, 645–678.

HOYAS, S. & JIMÉNEZ, J. 2006 Scaling of the velocity fluctuations in turbulent channels up to $Re_\tau = 2003$. *Phys. Fluids* **18**, 011702.

HU, R., YANG, X.I.A. & ZHENG, X. 2019 Wall-attached and wall-detached eddies in wall-bounded turbulent flows. *J. Fluid Mech.* **885**, A30.

HUNT, J.C.R. & FERNHOLZ, H. 1975 Wind-tunnel simulation of the atmospheric boundary layer: a report on Euromech 50. *J. Fluid Mech.* **70**, 543–559.

HUTCHINS, N. 2014 Large-scale structures in high Reynolds number wall-bounded turbulence. In *Progress in Turbulence V: Proceedings of the iTi Conference in Turbulence 2012* (ed. A. Talamelli, M. Oberlack & J. Peinke), pp. 75–83. Springer International Publishing.

HUTCHINS, N. & MARUSIC, I. 2007*a* Evidence of very long meandering features in the logarithmic region of turbulent boundary layers. *J. Fluid Mech.* **579**, 1–28.

HUTCHINS, N. & MARUSIC, I. 2007*b* Large-scale influences in near-wall turbulence. *Phil. Trans.* A*, Math. Phys. Engng Sci.* **365**, 647–664.

HUTCHINS, N., NICKELS, T.B., MARUSIC, I. & CHONG, M.S. 2009 Hot-wire spatial resolution issues in wall-bounded turbulence. *J. Fluid Mech.* **635**, 103.

IACOBELLO, G., RIDOLFI, L. & SCARSOGLIO, S. 2021 Large-to-small scale frequency modulation analysis in wall-bounded turbulence via visibility networks. *J. Fluid Mech.* **918**, A13.

ISHIHARA, T., GOTOH, T. & KANEDA, Y. 2009 Study of high–reynolds number isotropic turbulence by direct numerical simulation. *Annu. Rev. Fluid Mech.* **41**, 165–180.

ISHIHARA, T., KANEDA, Y., YOKOKAWA, M., ITAKURA, K. & UNO, A. 2007 Small-scale statistics in high-resolution direct numerical simulation of turbulence: Reynolds number dependence of one-point velocity gradient statistics. *J. Fluid Mech.* **592**, 335–366.

JIMÉNEZ, J., SIMENS, M., HOYAS, S. & MIZUNO, Y. 2008 Entry length requirements for direct simulations of turbulent boundary layers. Center for Turbulence Research, Annual Research Briefs 381–390.

JIMÉNEZ, J., WRAY, A.A., SAFFMAN, P.G. & ROGALLO, R.S. 1993 The structure of intense vorticity in isotropic turbulence. *J. Fluid Mech.* **255**, 65–90.

KIM, K.C. & ADRIAN, R.J. 1999 Very large-scale motion in the outer layer. *Phys. Fluids* **11**, 417.

KLEBANOFF, P.S. 1955 Characteristics of turbulence in a boundary layer with zero pressure gradient, NASA, Washington, DC.

KLEBANOFF, P.S. & DIEHL, Z.W. 1951 Some features of artificially thickened fully developed turbulent boundary layers with zero pressure gradient. *Tech. Rep.* 2475. DTIC Document.

KOVASZNAY, L.S.G., KIBENS, V. & BLACKWELDER, R.F. 1970 Large-scale motion in the intermittent region of a turbulent boundary layer. *J. Fluid Mech.* **41**, 283–325.

KUO, A.Y.-S. & CORRSIN, S. 1971 Experiments on internal intermittency and fine-structure distribution functions in fully turbulent fluid. *J. Fluid Mech.* **50**, 285–319.

KUZNETSOV, V.R., PRASKOVSKY, A.A. & SABELNIKOV, V.A. 1992 Fine-scale turbulence structure of intermittent hear flows. *J. Fluid Mech.* **243**, 595–622.

KWON, Y.S., HUTCHINS, N. & MONTY, J.P. 2016 On the use of the Reynolds decomposition in the intermittent region of turbulent boundary layers. *J. Fluid Mech.* **794**, 5–16.

LANDAU, L. & LIFSHITZ, E. 1963 *Fluid Mechanics*. Pergamon.

LI, M., BAARS, W.J., MARUSIC, I. & HUTCHINS, N. 2023 Quantifying inner-outer interactions in noncanonical wall-bounded flows. *Phys. Rev. Fluids* **8**, 084602.

LIGRANI, P.M. & BRADSHAW, P. 1987 Spatial resolution and measurement of turbulence in the viscous sublayer using subminiature hot-wire probes. *Exp. Fluids* **5**, 407–417.

LONG, Y., WU, D. & WANG, J. 2021 A novel and robust method for the turbulent/non-turbulent interface detection. *Exp. Fluids* **62**, 138.

MACHLUP, S. 1954 Noise in semiconductors: spectrum of a two-parameter random signal. *J. Appl. Phys.* **25**, 341–343.

MARUSIC, I., BAARS, W.J. & HUTCHINS, N. 2017 Scaling of the streamwise turbulence intensity in the context of inner-outer interactions in wall turbulence. *Phys. Rev. Fluids* **2**, 100502.

MARUSIC, I., CHAUHAN, K.A., KULANDAIVELU, V. & HUTCHINS, N. 2015 Evolution of zero-pressure-gradient boundary layers from different tripping conditions. *J. Fluid Mech.* **783**, 379–411.

MARUSIC, I., MCKEON, B.J., MONKEWITZ, P.A., NAGIB, H.M., SMITS, A.J. & SREENIVASAN, K.R. 2010 Wall-bounded turbulent flows at high Reynolds numbers: recent advances and key issues. *Phys. Fluids* **22**, 065103.

MARUSIC, I. & MONTY, J.P. 2019 Attached eddy model of wall turbulence. *Annu. Rev. Fluid Mech.* **51**, 49–74.

MARUSIC, I., MONTY, J.P., HULTMARK, M. & SMITS, A.J. 2013 On the logarithmic region in wall turbulence. *J. Fluid Mech.* **716**, R3.

MATHIS, R., HUTCHINS, N. & MARUSIC, I. 2009 Large-scale amplitude modulation of the small-scale structures in turbulent boundary layers. *J. Fluid Mech.* **628**, 311.

MATHIS, R., MARUSIC, I., CHERNYSHENKO, S.I. & HUTCHINS, N. 2013 Estimating wall-shear-stress fluctuations given an outer region input. *J. Fluid Mech.* **715**, 163–180.

MELDI, M., DJENIDI, L. & ANTONIA, R. 2018 Reynolds number effect on the velocity derivative flatness factor. *J. Fluid Mech.* **856**, 426–443.

MELLADO, J.P., WANG, L. & PETERS, N. 2009 Gradient trajectory analysis of a scalar field with external intermittency. *J. Fluid Mech.* **626**, 333–365.

MENEVEAU, C. & MARUSIC, I. 2013 Generalized logarithmic law for high-order moments in turbulent boundary layers. *J. Fluid Mech.* **719**, R1.

MENEVEAU, C. & SREENIVASAN, K.R. 1991 The multifractal nature of turbulent energy dissipation. *J. Fluid Mech.* **224**, 429–484.

METZGER, M.M. & KLEWICKI, J.C. 2001 A comparative study of near-wall turbulence in high and low Reynolds number boundary layers. *Phys. Fluids* **13**, 692–701.

MUSKER, A.J. 1979 Explicit expression for the smooth wall velocity distribution in a turbulent boundary layer. *AIAA J.* **17**, 655–657.

NAGIB, H.M. & CHAUHAN, K.A. 2008 Variations of von Kármán coefficient in canonical flows. *Phys. Fluids* **20**, 101518.

PEARSON, B.R. & ANTONIA, R.A. 2001 Reynolds-number dependence of turbulent velocity and pressure increments. *J. Fluid Mech.* **444**, 343–382.

PHILIP, J., MENEVEAU, C., DE SILVA, C.M. & MARUSIC, I. 2014 Multiscale analysis of fluxes at the turbulent/non-turbulent interface in high Reynolds number boundary layers. *Phys. Fluids* **26**, 015105.

POPE, S.B. 2000 *Turbulent Flows*. Cambridge University Press.

REUTHER, N. & KÄHLER, C.J. 2018 Evaluation of large-scale turbulent/non-turbulent interface detection methods for wall-bounded flows. *Exp. Fluids* **59**, 121.

RODRÍGUEZ-LÓPEZ, E., BRUCE, P.J.K. & BUXTON, O.R.H. 2015 A robust post-processing method to determine skin friction in turbulent boundary layers from the velocity profile. *Exp. Fluids* **56**, 68.

RODRÍGUEZ-LÓPEZ, E., BRUCE, P.J.K. & BUXTON, O.R.H. 2016*a* Near field development of artificially generated high Reynolds number turbulent boundary layers. *Phys. Rev. Fluids* **1**, 074401.

RODRÍGUEZ-LÓPEZ, E., BRUCE, P.J.K. & BUXTON, O.R.H. 2016*b* On the formation mechanisms of artificially generated high reynolds number turbulent boundary layers. *Boundary-Layer Meteorol.* **160**, 201–224.

RODRÍGUEZ-LÓPEZ, E., BRUCE, P.J.K. & BUXTON, O.R.H. 2017*a* Experimental measurement of wall shear stress in strongly disrupted flows. *J. Turbul.* **18**, 271–290.

RODRÍGUEZ-LÓPEZ, E., BRUCE, P.J.K. & BUXTON, O.R.H. 2017*b* Flow characteristics and scaling past highly porous wall-mounted fences. *Phys. Fluids* **29**, 075106.

SABELNIKOV, V.A., LIPATNIKOV, A.N., NISHIKI, S. & HASEGAWA, T. 2019 Investigation of the influence of combustion-induced thermal expansion on two-point turbulence statistics using conditioned structure functions. *J. Fluid Mech.* **867**, 45–76.

SANMIGUEL VILA, C., VINUESA, R., DISCETTI, S., IANIRO, A., SCHLATTER, P. & ÖRLÜ, R. 2017 On the identification of well-behaved turbulent boundary layers. *J. Fluid Mech.* **822**, 109–138.

SAXTON-FOX, T. & MCKEON, B.J. 2017 Coherent structures, uniform momentum zones and the streamwise energy spectrum in wall-bounded turbulent flows. *J. Fluid Mech.* **826**, R6.

SCHLATTER, P. & ÖRLÜ, R. 2010*a* Assessment of direct numerical simulation data of turbulent boundary layers. *J. Fluid Mech.* **659**, 116–126.

SCHLATTER, P. & ÖRLÜ, R. 2010*b* Quantifying the interaction between large and small scales in wall-bounded turbulent flows: a note of caution. *Phys. Fluids* **22**, 051704.

SCHLATTER, P. & ÖRLÜ, R. 2012 Turbulent boundary layers at moderate Reynolds numbers: inflow length and tripping effects. *J. Fluid Mech.* **710**, 5–34.

SEGALINI, A., ÖRLÜ, R. & ALFREDSSON, P.H. 2013 Uncertainty analysis of the von Kármán constant. *Exp. Fluids* **54**, 1460.

SILLERO, J.A., JIMÉNEZ, J. & MOSER, R.D. 2013 One-point statistics for turbulent wall-bounded flows at Reynolds numbers up to $\delta+ \approx 2000$. *Phys. Fluids* **25**, 105102.

DA SILVA, C.B., HUNT, J.C.R., EAMES, I. & WESTERWEEL, J. 2014 Interfacial layers between regions of different turbulence intensity. *Annu. Rev. Fluid Mech.* **46**, 567–590.

DE SILVA, C.M., KRUG, D., LOHSE, D. & MARUSIC, I. 2017 Universality of the energy-containing structures in wall-bounded turbulence. *J. Fluid Mech.* **823**, 498–510.

DE SILVA, C.M., MARUSIC, I., WOODCOCK, J.D. & MENEVEAU, C. 2015 Scaling of second- and higher-order structure functions in turbulent boundary layers. *J. Fluid Mech.* **769**, 654–686.

DE SILVA, C.M., PHILIP, J., CHAUHAN, K., MENEVEAU, C. & MARUSIC, I. 2013 Multiscale geometry and scaling of the turbulent-nonturbulent interface in high Reynolds number boundary layers. *Phys. Rev. Lett.* **111**, 044501.

SMITS, A.J. 2020 Some observations on Reynolds number scaling in wall-bounded flows. *Phys. Rev. Fluids* **5**, 110514.

SMITS, A.J. & MARUSIC, I. 2013 Wall-bounded turbulence. *Phys. Today* **66**, 25–30.

SMITS, A.J., MCKEON, B.J. & MARUSIC, I. 2011 High–Reynolds number wall turbulence. *Annu. Rev. Fluid Mech.* **43**, 353–375.

SREENIVASAN, K.R. & ANTONIA, R.A. 1997 The phenomenology of small-scale turbulence. *Annu. Rev. Fluid Mech.* **29**, 435–472.

SREENIVASAN, K.R. & MENEVEAU, C. 1986 The fractal facets of turbulence. *J. Fluid Mech.* **173**, 357–386.

TANG, S.L., ANTONIA, R.A., DJENIDI, L., DANAILA, L. & ZHOU, Y. 2018 Reappraisal of the velocity derivative flatness factor in various turbulent flows. *J. Fluid Mech.* **847**, 244–265.

TANG, Z., FAN, Z., CHEN, L. & JIANG, N. 2021 Outer-layer structure arrangements based on the large-scale zero-crossings at moderate Reynolds number. *Phys. Fluids* **33**, 085121.

TANG, Z. & JIANG, N. 2020 The effect of a synthetic input on small-scale intermittent bursting events in near-wall turbulence. *Phys. Fluids* **32**, 015110.

TANG, Z., JIANG, N., ZHENG, X. & WU, Y. 2016 Bursting process of large- and small-scale structures in turbulent boundary layer perturbed by a cylinder roughness element. *Exp. Fluids* **57**, 79.

TANG, Z., JIANG, N., ZHOU, Q. & LU, Z. 2024 Artificially thickened boundary layer turbulence due to trip wires of varying diameter. *Phys. Rev. Fluids* **9**, 024606.

THIESSET, F., DURET, B., MÉNARD, T., DUMOUCHEL, C., REVEILLON, J. & DEMOULIN, F.X. 2020 Liquid transport in scale space. *J. Fluid Mech.* **886**, A4.

TOWNSEND, A.A. 1976 *The Structure of Turbulent Shear Flow*. Cambridge University Press.

WANG, L., PAN, C., WANG, J. & GAO, Q. 2022 Statistical signatures of component wall-attached eddies in proper orthogonal decomposition modes of a turbulent boundary layer. *J. Fluid Mech.* **944**, A26.

WANG, L.-H., XU, C.-X., SUNG, H.J. & HUANG, W.-X. 2021 Wall-attached structures over a traveling wavy boundary: turbulent velocity fluctuations. *Phys. Rev. Fluids* **6**, 034611.

WANG, L.-P., CHEN, S., BRASSEUR, J.G. & WYNGAARD, J.C. 1996 Examination of hypotheses in the Kolmogorov refined turbulence theory through high-resolution simulations. Part 1. Velocity field. *J. Fluid Mech.* **309**, 113–156.

WATANABE, T., DA SILVA, C.B. & NAGATA, K. 2019 Non-dimensional energy dissipation rate near the turbulent/non-turbulent interfacial layer in free shear flows and shear free turbulence. *J. Fluid Mech.* **875**, 321–344.

WATANABE, T., DA SILVA, C.B. & NAGATA, K. 2020 Scale-by-scale kinetic energy budget near the turbulent/nonturbulent interface. *Phys. Rev. Fluids* **5**, 124610.

XIA, Z., BRETHOUWER, G. & CHEN, S. 2018 High-order moments of streamwise fluctuations in a turbulent channel flow with spanwise rotation. *Phys. Rev. Fluids* **3**, 022601.

YANG, X.I.A., MARUSIC, I. & MENEVEAU, C. 2016*a* Moment generating functions and scaling laws in the inertial layer of turbulent wall-bounded flows. *J. Fluid Mech.* **791**, R2.

YANG, X.I.A., MENEVEAU, C., MARUSIC, I. & BIFERALE, L. 2016*b* Extended self-similarity in moment-generating-functions in wall-bounded turbulence at high Reynolds number. *Phys. Rev. Fluids* **1**, 044405.

YOUNES, K., GIBEAU, B., GHAEMI, S. & HICKEY, J.-P. 2021 A fuzzy cluster method for turbulent/non-turbulent interface detection. *Exp. Fluids* **62**, 73.